

Carrier- and strain-tunable intrinsic magnetism in two-dimensional MAX_3 transition metal chalcogenides

Bheema Lingam Chittari,^{1,2} Dongkyu Lee,¹ Nepal Banerjee,¹ Allan H. MacDonald,³ Euyheon Hwang,^{2,*} and Jeil Jung^{1,†}

¹*Department of Physics, University of Seoul, Seoul 02504, Korea*

²*SKKU Advanced Institute of Nanotechnology, Sungkyunkwan University, Suwon, 16419, Korea*

³*Department of Physics, The University of Texas at Austin, Austin, Texas 78712, USA*



(Received 28 February 2018; revised manuscript received 11 November 2019; accepted 24 January 2020; published 20 February 2020)

We present a density functional theory study of the carrier-density and strain dependence of magnetic order in two-dimensional (2D) MAX_3 ($M = V, Cr, Mn, Fe, Co, Ni$; $A = Si, Ge, Sn$; and $X = S, Se, Te$) transition metal trichalcogenides. Our *ab initio* calculations show that this class of compounds includes wide and narrow gap semiconductors, metals, and half-metals, and that most of these compounds are magnetic. Although antiferromagnetic order is most common, ferromagnetism is predicted in $MSiSe_3$ for $M = Mn$ and Ni ; in $MSiTe_3$ for $M = V$ and Ni ; in $MnGeSe_3$; $MGeTe_3$ for $M = Cr, Mn$, and Ni ; in $FeSnS_3$; and in $MSnTe_3$ for $M = V, Mn$, and Fe . Among these compounds $CrGeTe_3$, $VSnTe_3$, and $CrSnTe_3$ are ferromagnetic semiconductors. Our calculations suggest that the competition between antiferromagnetic and ferromagnetic order can be substantially altered by strain engineering, and in the semiconductor case also by gating. The associated critical temperatures can be enhanced by means of carrier doping and strains.

DOI: [10.1103/PhysRevB.101.085415](https://doi.org/10.1103/PhysRevB.101.085415)

I. INTRODUCTION

2D materials research has now broadened beyond graphene [1,2] to include other classes of van der Waals materials [3] including transition metal chalcogenides (TMC) [4]. These materials can be metals or semiconductors, have exceptionally strong light-matter coupling, [5], and include ordered phases with charge density waves or superconductivity [6–9]. Because of their potential importance for nonvolatile information storage or logic device applications, the identification of two-dimensional (2D) materials with room-temperature magnetic order is an important research goal. Unfortunately, single-layer magnetism has so far been realized in only in relatively fragile 2D materials [10–15]. Other van der Waals magnetism systems have so far been thinned only to several layers [16–20], or prepared only in bulk form [21–37]. No single-layer 2D materials have been discovered that exhibit room-temperature magnetism.

Magnetic 2D materials that have been proposed theoretically over the last few years include tritellurides based on chromium such as $CrSiTe_3$ [38–43] and $CrGeTe_3$ [41–47], $CrSnTe_3$ [48], MPX_n ternary chalcogenophosphates [49–56], and transition metal tri- [31] and dichalcogenides [57–78]. The $CrATe_3$ ($A = Si, Ge$) [41] ternary tritellurides have been predicted to be bulk ferromagnets with small bulk band gaps. [21] Temperature dependent transport [14] and neutron scattering [22] measurements are suggestive of 2D magnetism in these materials. Transition temperature T_c estimates are de-

pendent on thickness, varying for example from 33 K for bulk $CrSiTe_3$ [14], to 80 K in monolayers, and exhibiting the opposite behavior in $CrGeTe_3$ layered materials where T_c decreases in thinner layers because of weak magnetic anisotropy [16]. Other nonchalcogenide transition metal magnetic layered materials like the tri- [79–87] and dihalides [88–92] are expected to be ferromagnetic semiconductors with Curie temperatures typically below one hundred degrees Kelvin. A recent breakthrough experiment has demonstrated CrI_3 devices in ultrathin layered form and revealed an intricate competition between ferromagnetic (FM) and antiferromagnetic (AFM) states as a function of layer number and external field [15].

In this paper, we present a DFT survey of the magnetic phases of MAX_3 single-layer transition metal trichalcogenide compounds covering a variety 3d transition metals ($M = V, Cr, Mn, Fe, Co$, and Ni), the group IV elements ($A = Si, Ge$, and Sn), and the three chalcogen atoms ($X = S, Se$, and Te). These single-layer compounds are structurally closely related to their transition metal trichalcogenide MPX_3 cousins, which we studied in a recent related paper [54]. The main difference between MAX_3 and MPX_3 compounds is that the group V phosphorus (P) atom inside the $(P_2X_6)^{4-}$ skeleton are replaced by $(A_2X_6)^{6-}$ bipyramids with group IV elements $A = (Si, Ge, \text{ and } Sn)$. The change from P to a group IV element is responsible for important modifications in electronic and magnetic properties. We have examined the magnetic phase competitions between ferromagnetic (FM) and a variety antiferromagnetic (AFM) states, and the competition between magnetic and nonmagnetic (NM) phases, as a function of electron carrier density and strain. While density functional theory does not always reliably capture the correlations present in transition metal compounds, we expect that our

*euyheon@skku.edu

†jeiljung@uos.ac.kr

study, which is carried out under a unified framework, should provide useful insight into property trends in this class of materials.

Our paper is structured as follows. In Sec. II, we summarize the technical details of our first principles electronic structure calculations. In Sec. III, we discuss results for ground-state properties including structure, magnetic properties, and electronic band structures and densities-of-states. In Sec. IV, we analyze the carrier-density dependence and the influence of strain on the magnetic phase competition. Finally, in Sec. V, we close the paper with the summary and discussions.

II. AB INITIO CALCULATION DETAILS

The calculations described in this paper were carried out using the plane-wave DFT software QUANTUM ESPRESSO [93] to obtain ground-state electronic structure using ultrasoft pseudopotentials (RRKJUS) for the semilocal PBE-GGA [94]. We have in addition added vdW-D2 [95] corrections to perform GGA+D2 (hereafter DFT-D2) calculations as a reference calculation thought to provide a description of the in-plane covalent bonds that is improved relative to the LDA [96], and to add a weak interlayer binding correction through the D2 contribution [97]. We have also corrected onsite repulsion by performing GGA+D2+ U calculations (hereafter referred to as DFT-D2+ U), normally assuming the value $U = 4$ eV. In a few select cases involving Co and Ni metals, we have used larger values of U in order to obtain ground states that are magnetic. In all cases, the atomic structure has been optimized by relaxing forces below 10^{-5} Ry/a.u., while the total energy tolerance for the self-consistency was set to 10^{-10} Ry. The k -point sampling density used a regularly spaced $4 \times 8 \times 1$ k -point grid and the plane wave cutoff energy was set to 60 Ry. Out-of-plane supercell periods of 25 Å allowed for a vacuum spacing in excess of 15 Å between facing chalcogen atoms, making overlaps between the electron clouds associated with different layers negligible.

III. STRUCTURAL AND MAGNETIC PROPERTIES

The MAX_3 transition metal trichalcogenide layers consist of $3d$ transition metals $M = (V, Cr, Mn, Fe, Co, \text{ and } Ni)$ anchored by $(A_2X_6)^{6-}$ bipyramid ions with $X = (S, Se, \text{ and } Te)$ and $A = (Si, Ge, \text{ and } Sn)$. The 12 electrons taken by the six chalcogen atoms per unit cell are partly compensated by the six electrons needed by sp^3 bonds with bridge A atoms, leaving a final 6^- valence state for the anionic enclosure. The triangular lattice of bipyramids provides enclosures for the transition metal atoms, forming a structure that is practically identical to that of MPX_3 compounds enclosed by $(P_2X_6)^{4-}$ bipyramids. The octahedral arrangement of the chalcogens surrounding the metal ions is expected to give rise to crystal or ligand exchange fields [98] that split the d orbitals into triply degenerate t_{2g} and doubly degenerate e_g levels which can further split in the presence of distortions as illustrated schematically in Fig. 1. The main difference between MAX_3 and MPX_3 compounds is that the A atoms have one fewer

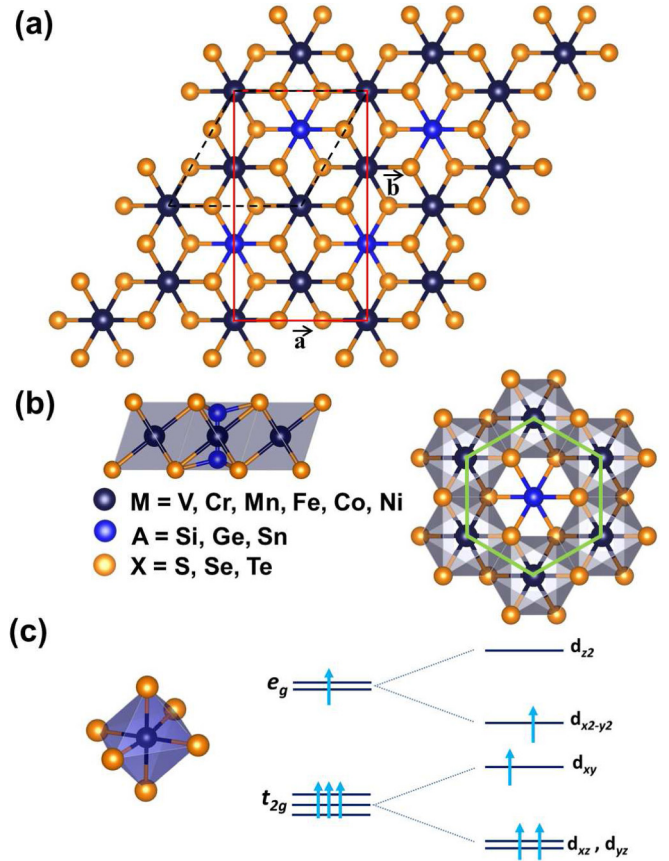


FIG. 1. Schematic representation of the atomic structure of MAX_3 compounds. (a) Atomic structure of a MAX_3 monolayer identifying two possible choices for the unit cells, a rectangular cell identified by red lines containing four transition metal atoms (M), and a smaller triangular cell identified by black dashed lines containing two transition metal atoms (M). (b) Side and top views of single-layer MAX_3 compound. The MAX_3 compounds have one fewer occupied band than MPX_3 compounds because of the replacement of P atom pairs by group IV atoms (A) pairs that have with one fewer valence electron. The M atoms form hexagons (light green lines) centered by the A ($= Si, Ge, \text{ and } Sn$) bright blue atoms which are in turn surrounded two pairs of chalcogen X ($= S, Se, \text{ and } Te$) triangles represented in orange. (c) Schematic illustration of the octahedral ligands that give rise to lower energy t_{2g} and higher energy e_g metal atom d orbitals. The t_{2g} and e_g degeneracies are lifted by lattice distortions, for example, as illustrated by z -axis elongation of the octahedron.

electron compared to P atoms yielding compounds with larger nominal metal cation valences, 3^+ in MAX_3 compounds versus 2^+ in the MPX_3 compounds. The magnetic moments are carried largely by the metal ions, but the interactions between moments is dependent on their hybridizations with both the chalcogens and the A bridge atoms. All the 2D MAX_3 crystals we considered are magnetically ordered within DFT-D2, except for $CoAX_3$, $NiGeS_3$, and $NiSnX_3$. These become magnetic only within DFT-D2+ U and only for a sufficiently large onsite repulsion parameter. Figure 2 summarizes the overall trends in magnetic condensation energy, i.e., in the energy gained by forming a magnetically ordered states. These results

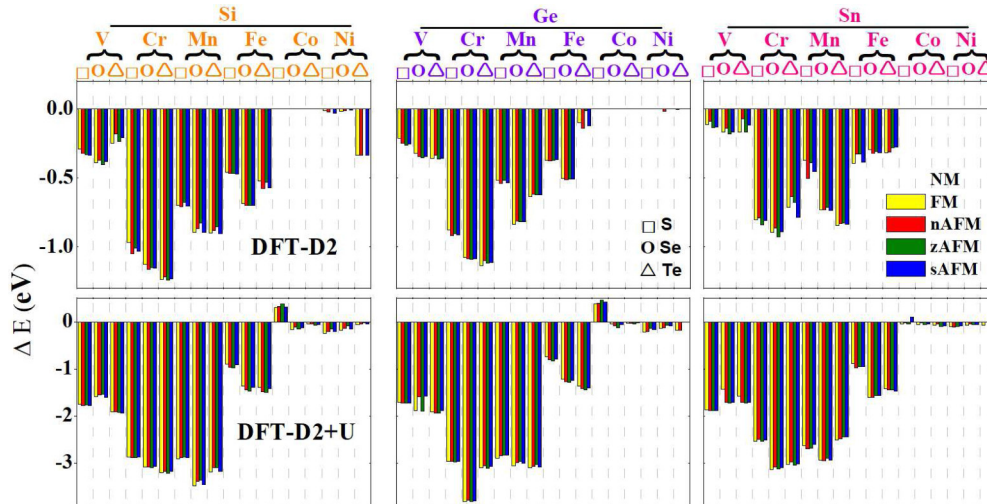


FIG. 2. Magnetic condensation energy trends. The energy gained per metal atom due to magnetic order obtained within DFT-D2 and DFT-D2+ U ($= 4$ eV). In the cases of CoATe_3 , CoASe_3 ($A = \text{Ge}$ and Sn), and CoSnS_3 , we choose the U parameter values of 5, 6, and 7 eV, respectively, in order to obtain a magnetic ground state. Energy differences are not shown for cases in which metastable magnetic solutions could not be obtained.

show a strong tendency for magnetism for Cr compounds in which the t_{2g} bands are close to half-filling, and weak in Co compounds in which the t_{2g} bands are filled. It is clear therefore that crystal field effects play a strong role in the magnetism of these compounds. In the following, we present an analysis of the structural, magnetic, and electronic properties of representative 2D transition metal MAX_3 trichalcogenides, emphasizing their dependence on the chalcogen element (Si, Ge, and Sn) and their underlying electronic band structures.

A. Atomic structure of the lattice

The atomic structure in the single-layer limit have been obtained by relaxing the structures using rectangular unit cells defined by two perpendicular vectors that we label with a and b , see Fig. 1, and an additional layer thickness c' parameter defined as the distance between the chalcogen atom planes of the same MAX_3 single layer sandwiching the metal ions. The relaxed structures both for in-plane lattice constants and layer thickness of the rectangular unit cells, as obtained using DFT-D2 (Fig. S1 and Table I in Ref. [99]), are found to increase for larger chalcogen atoms for given A (Si, Ge, and Sn) atoms. In general the calculated self-consistent lattice constants depend on the magnetic ordering. The variation is substantial for the transition metals V, Cr, Mn, and Fe for all combinations of A (Si, Ge, and Sn) and chalcogens S, Se, and Te, up to 10% for in-plane lattice constants and up to 20% for the layer thickness, see Fig. 3. For compounds with Co and Ni the lattice distortions are much smaller. As a rule of thumb we can see that the magnitude in the distortion of the bonds is roughly proportional to the total energy differences represented in Fig. 2 and therefore they are largest when we compare magnetic and nonmagnetic phases. As in the MPX_3 compounds [54], we observe that the interplay between atomic structure and magnetic properties is strong. This interdependence between lattice structure and magnetic phases suggests the possibility of changing the magnetic phases

through strains as we will discuss later on. In addition to the DFT-D2 calculations, we have optimized all the structures within DFT-D2+ U in the presence of local electron repulsion introduced through Hubbard U . The onsite repulsion will tend to lower/raise the occupied/empty spin-polarized energy levels and often lead to further splitting of the conduction and valence d orbitals. The introduction of U leads to total energy differences between magnetic and nonmagnetic phases that are roughly doubled (see Fig. 2) within DFT-D2+ U when compared to DFT-D2, and this difference is reflected in the increase of the lattice distortions. The relative difference of the lattice parameters between DFT-D2+ U and DFT-D2 geometries are comparable to the difference between magnetic and nonmagnetic phases within the same DFT approximation, see Fig. 3 and Fig. S1 in Ref. [99]. This observation indicates that the short-range correlations of the transition metal atoms will generally impact the ground-state magnetic properties.

B. Magnetic configurations

The magnetic ground-state and metastable magnetic configurations are obtained by identifying energy extrema via converged self-consistency using initial conditions corresponding to Néel antiferromagnetic (nAFM), zigzag antiferromagnetic (zAFM), stripy antiferromagnetic (sAFM), ferromagnetic (FM), and nonmagnetic (NM) states. The analysis of the magnetic ground states obtained for the single-layer MAX_3 compounds indicate that the magnetic moments are usually concentrated mostly at the metal atoms for AFM phases, a fact that simplifies our analysis of the magnetic solutions based on effective models. However, when the magnetic configuration is ferromagnetic we observe that a non-negligible spin polarization develop at the group IV and chalcogen atom sites of $0.3 \mu_B$ – $0.8 \mu_B$ in CrSiX_3 . The specific magnetic solution will depend on the orbital hybridization between the metal ion and surrounding atoms to either suppress or enhance the tendency of the $3d$ transition metal elements to order magnetically.

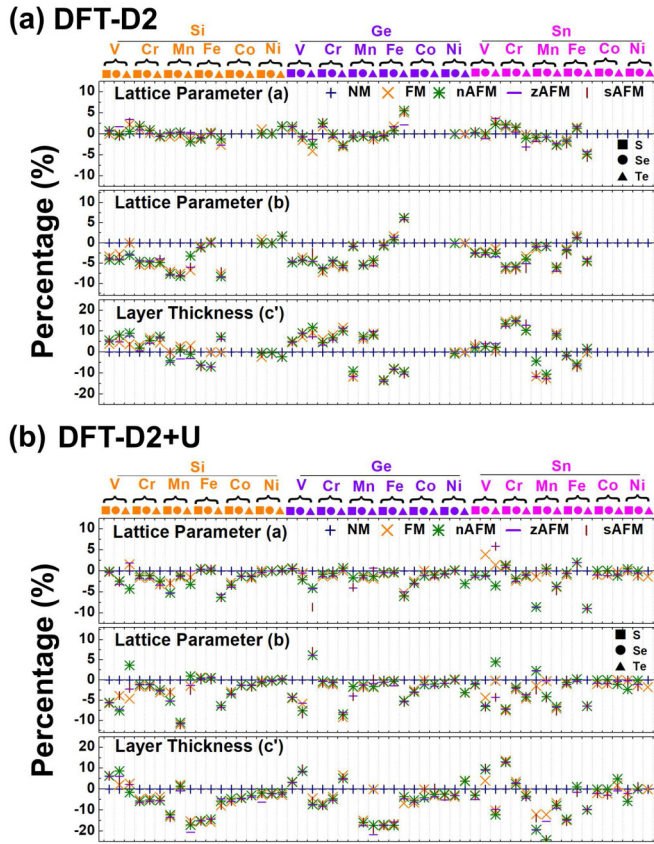


FIG. 3. Relative distortion of the lattice parameter for different magnetic phases FM, nAFM, zAFM, and sAFM measured with respect to the structural parameters obtained for nonmagnetic phases using a rectangular unit cell with in-plane lattice parameters a (Å) and b (Å), and layer thickness c' (Å). The negative and positive values represent respectively compression and expansion during this nonmagnetic to magnetic transition. (a) Calculations within DFT-D2 and (b) within DFT-D2+ U . The latter shows generally greater variations in the lattice constants.

As discussed earlier, the transition metal atoms in 2D MAX_3 crystals can be viewed as contained in bipyramidal molecular cages formed by group IV A (Si, Ge, Sn) atoms and chalcogens that interact with the metal atoms. The relatively weak hybridization between the neighboring transition metal atom orbitals indicate that the intermetal exchange interactions is mediated indirectly through the intermediate atoms. We have estimated the exchange interactions from *ab initio* electronic structure calculations from the total energies corresponding to antiferromagnetic, ferromagnetic, and nonmagnetic phases, see Fig. 2. In Tables I–III in Ref. [99], we present the numerical values for the total energies corresponding to the different magnetic configurations. Our results indicate that the magnetic phases are normally favored over the nonmagnetic solutions. Exceptions to this rule are the nonmagnetic phases predicted within DFT-D2 for $CoAX_3$, $NiGeS_3$, and $NiSnX_3$. These compounds do develop magnetic solutions when we use a sufficiently large onsite repulsion parameter U within DFT-D2+ U . We have generally used the $U = 4$ eV value to assess the role of onsite Coulomb repulsion on the magnetic ground state energies, and used larger values ($U = 5$ eV for

$CoGeTe_3$, $CoSnTe_3$, $U = 6$ eV for $CoGeSe_3$, $CoSnSe_3$, and $U = 7$ eV for $CoSnS_3$) to obtain magnetic solutions when they did not appear for $U = 4$ eV. Our DFT calculations predict that the Ni based trichalcogenides are magnetic only for some of the considered spin configurations. For instance, $NiGeS_3$ and $NiSnX_3$ are nonmagnetic within DFT-D2, and zAFM and sAFM phases are missing in $NiSiX_3$ and $NiGeSe_3$, and $NiGeTe_3$ has only ferromagnetic ordering. Within DFT-D2+ U it is possible to obtain both FM and nAFM for $NiGeTe_3$, and FM only for $NiSnTe_3$.

By considering that the magnetic moments are almost entirely located at the metal atoms in a honeycomb array we write the total energies per metal atom using an effective classical spin Hamiltonian as follows:

$$H = - \sum_{(ij)} J_{ij} \vec{S}_i \cdot \vec{S}_j = - \frac{1}{2} \sum_{i \neq j} J_{ij} \vec{S}_i \cdot \vec{S}_j, \quad (1)$$

where the coefficients J_{ij} represent the exchange coupling between two metal atom sites, the \vec{S}_i represents the spin magnetic moment at the metal atom site labeled by i . We take semi-integer values $S = M/g\mu_B$ for spin magnitudes, where M represents the magnetic moments per metal atom for single-layer magnetic MAX_3 structures and $g = 2$. This notation convention is different from a previous work on MPX_3 [54] resulting in J parameters that are four times larger and have reversed sign. The double-counting of the interactions are corrected by the 1/2 prefactor in Eq. (1). From the total energies for a unit cell with four metal atoms corresponding to ferromagnetic (FM), Néel (nAFM), zigzag AFM (zAFM), and stripy AFM (sAFM) configurations shown in Fig. 4 [49,100], and assuming a relatively short-ranged magnetic interactions consisting of three J_1 , J_2 , and J_3 parameters we can obtain

$$E_{FM} - E_{AFM} = 3(J_1 + J_3) \vec{S}_A \cdot \vec{S}_B, \quad (2)$$

$$E_{zAFM} - E_{sAFM} = (J_1 - 3J_3) \vec{S}_A \cdot \vec{S}_B, \quad (3)$$

$$E_{FM} + E_{AFM} - E_{zAFM} - E_{sAFM} = 8J_2 \vec{S}_A \cdot \vec{S}_A, \quad (4)$$

where in the above equations we used the spin vectors $\vec{S}_{A/B}$ in dimensionless units acting on the triangular sublattices A and B in a honeycomb lattice.¹ The average magnetic moments in units of μ_B calculated within DFT-D2 and DFT-D2+ U are presented in Table I. The list of J parameters for all the MAX_3 compounds are in Table II. We notice that for MAX_3 compounds where $A = Si$ we get numerical values for the magnetization at V, Cr, Mn, and Fe sites close to 2, 3, 4, and 1 μ_B , while for $A = Ge$, and Sn, we get 2, 3, 3, and 1 μ_B . Counting the number of 3d electrons filling of the t_{2g} and e_g bands, we can make sense of the total magnetization dependence on the number of valence electrons. We note that the atomic 4s levels of the transition metal atoms in the 3⁺ cations lie higher up in energy than the 3d levels and they can

¹Here we use \vec{S} for spins rather than magnetic moments as in Ref. [54]. Due to the absence of the implicit $g = 2$ factor the J parameters in this work are defined to be a factor of four times greater than in the previous reference for MPX_3 compounds.

TABLE I. Magnetic moments in Bohr magneton μ_B per metal atom for single-layer magnetic MAX_3 structures, magnetic anisotropy energy (MAE) in μV as the total energy difference for spins in the easy and hard axes where $\theta = 0^\circ$ is parallel to out of the plane axis- z . In the cases of $CoATe_3$, $CoASe_3$ ($A = Ge, Sn$), and $CoSnS_3$ the U parameter values used are 5, 6, and 7 eV, respectively. We use the labels of FM for ferromagnetic, nAFM for Néel antiferromagnetic, zAFM for zigzag antiferromagnetic, and sAFM for stripy antiferromagnetic configurations. The *ab initio* calculations were performed within DFT-D2 and DFT-D2+ U .

MAX_3	DFT-D2							DFT-D2+ U						
	FM	nAFM	zAFM	sAFM	MAE	θ_{easy}	θ_{hard}	FM	nAFM	zAFM	sAFM	MAE	θ_{easy}	θ_{hard}
$VSiS_3$	1.683	1.483	1.560	1.525	249.2	85°	0°	1.903	1.880	1.903	1.874	194.6	90°	0°
$VSiSe_3$	1.787	1.546	1.650	1.590	129.4	60°	0°	2.466	2.612	2.607	2.409	84.2	0°	90°
$VSiTe_3$	1.932	1.768	1.890	1.895	865.6	0°	65°	2.792	2.792	2.756	2.806	6524.0	0°	90°
$CrSiS_3$	2.759	2.604	2.640	2.615	241.4	90°	0°	3.183	3.147	3.173	3.141	33.0	90°	0°
$CrSiSe_3$	2.773	2.701	2.734	2.794	65.0	0°	90°	3.430	3.406	3.433	3.394	272.8	0°	90°
$CrSiTe_3$	2.851	2.794	3.076	3.031	342.2	0°	90°	3.733	3.724	3.750	3.708	1063.4	0°	90°
$MnSiS_3$	3.612	3.423	3.503	3.553	4.4	0°	90°	4.232	4.468	4.453	4.234	19.6	0°	90°
$MnSiSe_3$	3.661	3.629	3.671	3.606	902.6	90°	0°	4.313	4.256	4.339	4.297	380.2	90°	0°
$MnSiTe_3$	3.741	3.719	3.765	3.660	7517.8	90°	0°	4.410	4.443	4.463	4.396	11706.0	90°	0°
$FeSiS_3$	0.983	1.025	1.013	1.012	304.6	90°	25°	3.696	3.644	3.570	3.677	900.4	85°	0°
$FeSiSe_3$	1.082	1.149	1.143	1.121	617.8	0°	90°	3.557	3.510	3.560	3.547	2167.8	0°	90°
$FeSiTe_3$	1.160	1.247	1.230	1.190	629.2	0°	90°	3.356	3.407	3.368	3.284	795.4	0°	75°
$CoSiS_3$	—	—	—	—	—	—	—	2.181	2.220	2.264	2.205	44.8	55°	90°
$CoSiSe_3$	—	—	—	—	—	—	—	1.200	1.241	1.254	1.202	617.0	0°	90°
$CoSiTe_3$	—	—	—	—	—	—	—	1.145	1.169	1.209	1.183	1170.4	0°	90°
$NiSiS_3$	0.699	0.573	—	0.611	—	—	—	1.013	1.008	0.885	0.993	35.6	0°	80°
$NiSiSe_3$	0.646	0.491	—	0.546	—	—	—	0.929	0.881	0.847	0.885	11.8	10°	90°
$NiSiTe_3$	0.323	0.306	—	0.274	—	—	—	0.739	0.632	0.503	0.649	0.02	15°	90°
$VGeS_3$	1.651	1.473	1.514	1.506	232.8	90°	0°	1.907	1.865	1.887	1.870	158.4	90°	0°
$VGeSe_3$	1.660	1.532	1.575	1.653	52.8	50°	0°	2.083	2.602	2.109	2.599	122.6	90°	35°
$VGeTe_3$	1.899	1.700	1.851	1.830	64.4	0°	50°	2.824	2.789	2.797	2.832	2731.0	0°	90°
$CrGeS_3$	2.675	2.597	2.624	2.610	22.6	90°	0°	3.100	3.130	3.155	3.137	30.4	90°	0°
$CrGeSe_3$	2.758	2.688	2.717	2.703	118.2	0°	90°	3.421	3.387	3.418	3.394	182.6	0°	90°
$CrGeTe_3$	3.078	2.774	2.803	3.024	56.4	55°	0°	3.725	3.709	3.733	3.708	344.8	0°	90°
$MnGeS_3$	2.798	2.529	2.654	2.587	306.6	90°	0°	4.108	4.093	4.461	4.464	264.0	90°	0°
$MnGeSe_3$	2.980	2.879	2.887	2.852	2205.8	90°	0°	4.225	4.200	4.214	4.203	9831.6	90°	0°
$MnGeTe_3$	3.331	3.155	3.183	3.235	12358.8	90°	0°	4.364	4.353	4.445	4.435	19606.8	90°	0°
$FeGeS_3$	0.966	1.013	0.992	0.994	23.2	90°	0°	3.617	3.639	3.650	3.598	1265.6	90°	0°
$FeGeSe_3$	1.050	1.135	1.103	1.104	491.0	0°	75°	3.549	3.576	3.506	3.530	3188.0	90°	0°
$FeGeTe_3$	1.141	1.230	1.224	1.210	402.2	50°	0°	3.356	3.409	3.367	3.425	5678.2	90°	0°
$CoGeS_3$	—	—	—	—	—	—	—	2.144	2.170	2.194	2.166	84.2	55°	25°
$CoGeSe_3$	—	—	—	—	—	—	—	0.854	1.188	1.243	0.919	310.8	50°	90°
$CoGeTe_3$	—	—	—	—	—	—	—	1.077	1.036	1.189	0.864	3616.2	55°	0°
$NiGeS_3$	—	—	—	—	—	—	—	0.981	0.973	0.897	0.949	498.2	20°	65°
$NiGeSe_3$	0.499	0.518	0.197	—	—	—	—	0.903	0.856	0.807	0.822	81.2	25°	0°
$VSnS_3$	1.576	1.302	1.312	1.509	93.4	90°	0°	1.871	1.831	1.852	1.842	764.2	85°	0°
$VSnSe_3$	1.619	1.414	1.447	1.575	351.6	0°	90°	2.104	1.948	1.983	2.014	403.2	80°	0°
$VSnTe_3$	1.602	1.466	1.660	1.611	1340.2	0°	90°	2.673	2.812	2.851	2.839	4846.2	90°	0°
$CrSnS_3$	2.623	2.545	2.549	2.549	57.0	0°	90°	3.059	3.020	3.033	3.024	12.0	80°	5°
$CrSnSe_3$	2.692	2.622	2.704	2.731	3872.0	0°	90°	3.319	3.292	3.301	3.293	216.6	75°	45°
$CrSnTe_3$	2.894	2.895	2.825	2.937	1083.0	70°	0°	3.805	3.786	3.822	3.808	393.2	75°	0°
$MnSnS_3$	2.799	2.392	2.573	2.421	2166.0	0°	90°	4.099	3.964	3.983	4.043	272.2	90°	0°
$MnSnSe_3$	3.043	2.750	2.867	2.823	2943.4	90°	0°	4.226	4.174	4.210	4.159	5076.6	90°	0°
$MnSnTe_3$	3.260	3.003	3.183	3.153	2432.6	90°	0°	4.458	4.456	4.473	4.464	27725.4	90°	0°
$FeSnS_3$	0.929	0.938	0.924	0.947	2816.4	0°	85°	3.665	3.596	3.583	3.553	43.8	60°	0°
$FeSnSe_3$	0.991	1.014	0.986	1.013	54.8	0°	90°	3.446	3.444	3.466	3.449	4086.4	90°	0°
$FeSnTe_3$	1.088	1.193	1.114	1.170	2103.2	90°	15°	3.117	3.043	2.932	3.111	3760.6	90°	20°
$CoSnS_3$	—	—	—	—	—	—	—	0.914	0.593	0.913	2.042	929.4	0°	90°
$CoSnSe_3$	—	—	—	—	—	—	—	1.024	0.663	1.046	1.044	3209.2	0°	90°
$CoSnTe_3$	—	—	—	—	—	—	—	0.855	0.638	1.117	1.090	2719.8	10°	90°
$NiSnS_3$	—	—	—	—	—	—	—	0.755	0.666	0.674	0.638	4.4	90°	0°
$NiSnSe_3$	—	—	—	—	—	—	—	0.789	0.275	0.685	0.524	7.0	70°	0°

TABLE II. Magnetization ($M/\mu_B = gS$) per metal atom for single-layer magnetic MAX_3 structures, the three nearest-neighbor exchange coupling strengths J_i in meV implied by the Heisenberg model mapping, and Monte Carlo estimates of the single-layer critical temperatures based on the Heisenberg with magnetic anisotropy with $E_{\text{ani}}(\theta)$ and the Ising limit of the classical spin model. The T_c for the *ab initio* calculations were performed within DFT-D2 and DFT-D2+ U .

MAX_3	DFT-D2						DFT-D2+ U					
	gS	J_1	J_2	J_3	Heisenberg T_c	Ising T_c	gS	J_1	J_2	J_3	Heisenberg T_c	Ising T_c
VSiS ₃	1.562	-15.24	-11.02	-3.256	37.1	75.6	1.890	-8.552	-0.920	-1.240	35.2	123.5
VSiSe ₃	1.643	13.76	-3.704	-4.924	31.1	121.6	2.523	-7.052	-0.052	13.46	135.5	483.7
VSiTe ₃	1.871	28.44	-1.468	-1.272	84.4	321.2	2.786	-1.568	-2.144	1.488	30.6	115.6
CrSiS ₃	2.654	-13.97	-1.448	-0.800	45.0	46.4	3.161	-0.960	0.002	-1.004	35.7	116.0
CrSiSe ₃	2.750	-6.788	-1.116	-0.964	92.3	160.1	3.415	2.852	-0.108	-1.700	32.4	126.3
CrSiTe ₃	2.938	3.576	-1.000	-0.104	5.1	27.3	3.728	5.064	0.008	-2.388	43.6	188.5
MnSiS ₃	3.522	-2.820	1.000	1.920	30.1	118.8	4.346	0.928	0.920	0.896	132.2	432.2
MnSiSe ₃	3.641	-2.876	1.528	5.660	109.5	361.8	4.301	-0.064	1.556	6.580	345.4	1098.0
MnSiTe ₃	3.721	-1.884	0.796	4.076	68.2	260.9	4.428	1.056	0.684	5.284	286.9	932.1
FeSiS ₃	1.008	-10.95	-6.804	2.052	8.8	35.8	3.646	0.736	-1.300	-6.916	150.4	529.2
FeSiSe ₃	1.123	-9.608	-4.760	-4.208	36.2	38.8	3.543	0.144	-1.748	-8.956	178.2	635.0
FeSiTe ₃	1.206	-65.57	-2.616	17.69	13.9	95.1	3.353	-1.476	-1.920	-8.656	144.8	522.7
CoSiS ₃	-	-	-	-	-	-	2.217	-4.896	6.508	13.91	200.1	672.1
CoSiSe ₃	-	-	-	-	-	-	1.224	43.54	-0.560	-3.620	62.6	225.1
CoSiTe ₃	-	-	-	-	-	-	1.176	7.036	-11.97	-7.908	28.7	108.6
NiSiS ₃	-	-	-	-	-	-	0.974	-22.54	42.58	70.19	244.6	797.9
NiSiSe ₃	-	-	-	-	-	-	0.885	-26.42	53.46	92.20	266.0	859.2
NiSiTe ₃	-	-	-	-	-	-	0.630	-7.392	41.96	-39.58	103.5	333.3
VGeS ₃	1.536	-12.02	-10.76	-9.112	27.3	108.2	1.882	-5.184	-1.244	-1.408	16.7	56.6
VGeSe ₃	1.536	-4.512	-6.848	-6.512	29.7	105.4	2.348	111.6	0.696	-40.33	109.1	901.0
VGeTe ₃	1.820	7.876	-3.848	0.872	8.8	40.8	2.810	3.672	2.040	-8.788	136.0	365.3
CrGeS ₃	2.626	-7.104	-1.296	-0.884	39.9	130.0	3.130	0.904	-0.204	-0.356	7.4	29.2
CrGeSe ₃	2.716	-1.156	-1.032	-0.660	5.5	18.1	3.405	3.756	-0.460	-0.704	39.4	43.6
CrGeTe ₃	2.919	4.712	-0.116	0.972	64.5	230.2	3.718	5.956	-0.672	-1.372	17.6	117.4
MnGeS ₃	2.642	-6.276	-0.032	1.780	13.4	63.1	4.281	2.720	1.980	0.840	252.5	832.3
MnGeSe ₃	2.899	2.400	0.536	1.320	71.4	239.1	4.210	0.608	2.240	3.636	310.1	988.2
MnGeTe ₃	3.226	1.636	0.564	0.772	64.9	221.4	4.399	-0.912	1.532	2.664	183.4	586.7
FeGeS ₃	0.991	-1.008	7.564	-7.256	46.8	147.1	3.626	-2.036	-3.144	-4.672	107.2	380.6
FeGeSe ₃	1.098	-6.124	0.580	-6.128	29.7	96.5	3.540	-1.276	-2.192	-4.232	91.4	322.1
FeGeTe ₃	1.201	-106.0	34.47	65.20	135.1	552.8	3.389	-1.756	-3.332	-4.060	84.8	305.4
CoGeS ₃	-	-	-	-	-	-	2.168	-6.284	-11.45	8.244	99.3	369.0
CoGeSe ₃	-	-	-	-	-	-	1.051	27.27	-23.11	-75.90	159.2	547.7
CoGeTe ₃	-	-	-	-	-	-	1.041	34.31	-3.104	-24.76	47.3	177.8
NiGeS ₃	-	-	-	-	-	-	0.95	-2.548	63.52	32.33	270.6	889.4
NiGeSe ₃	-	-	-	-	-	-	0.847	-4.224	74.67	28.408	233.0	765.0
VSnS ₃	1.424	14.77	-15.54	1.908	24.6	77.9	1.849	-3.012	-2.576	-2.412	10.6	40.8
VSnSe ₃	1.513	18.66	-9.336	-1.884	20.8	95.1	2.012	-59.40	-32.52	-23.64	61.7	276.7
VSnTe ₃	1.584	57.10	-8.336	-5.668	15.7	140.6	2.793	-17.14	-9.720	-6.352	38.9	123.5
CrSnS ₃	2.566	7.100	-4.308	-4.060	70.7	259.9	3.034	7.240	-0.660	-0.920	5.1	112.3
CrSnSe ₃	2.687	8.748	-3.956	-3.548	66.2	262.7	3.301	7.352	-0.636	-0.792	6.0	166.2
CrSnTe ₃	2.887	-4.092	-6.668	16.20	255.8	901.0	3.805	5.956	-1.788	-0.080	11.6	69.6
MnSnS ₃	2.546	-29.88	2.368	3.056	24.6	95.6	4.022	1.996	1.196	-6.640	181.5	596.9
MnSnSe ₃	2.870	-3.132	0.768	2.628	254.4	914.4	4.192	-2.768	1.416	1.800	85.8	301.7
MnSnTe ₃	3.149	0.364	0.420	1.460	19.0	167.1	4.462	1.908	2.372	0.592	268.3	883.8
FeSnS ₃	0.934	10.37	2.824	94.86	165.2	554.7	3.599	-7.276	-1.452	-3.248	143.4	483.7
FeSnSe ₃	1.001	22.97	-32.87	17.26	36.2	98.8	3.451	-0.596	3.672	0.600	101.7	441.9
FeSnTe ₃	1.141	-1.308	29.14	3.868	36.2	457.7	3.050	-11.64	-0.980	1.020	66.3	243.7
CoSnS ₃	-	-	-	-	-	-	1.115	137.6	48.66	-106.7	64.9	340.2
CoSnSe ₃	-	-	-	-	-	-	0.944	52.69	-19.90	6.744	7.8	46.2
CoSnTe ₃	-	-	-	-	-	-	0.925	42.31	-33.22	-1.128	16.2	75.2
NiSnS ₃	-	-	-	-	-	-	0.683	6.216	37.22	-37.38	98.8	113.7
NiSnSe ₃	-	-	-	-	-	-	0.568	117.8	-22.32	20.264	34.8	316.6

TABLE III. Band gaps and electronic property of MAX_3 compounds. The band gaps are listed in eV energy units and their values and the magnetic configuration depend substantially on the exchange-correlation approximation employed within DFT-D2 and DFT-D2+ U ($= 4$ eV). For $CoATe_3$, $CoAsSe_3$ ($A = Ge, Sn$), and $CoSnS_3$, the U parameter values chosen are 5, 6, and 7 eV, respectively. Different calculation methods have been indicated by I:DFT-D2 and II:DFT-D2+ U . The ground states for selected method are represented in boldface type and blue color (M:metal; SM:semimetal; and HM:half-metal). We distinguish the different magnetic configurations nonmagnetic (NM), ferromagnetic (FM), Néel antiferromagnetic (nAFM), zigzag antiferromagnetic (zAFM), and stripy antiferromagnetic (sAFM).

A	Method	Si					Ge					Sn				
		NM	FM	nAFM	zAFM	sAFM	NM	FM	nAFM	zAFM	sAFM	NM	FM	nAFM	zAFM	sAFM
VAS ₃	I	M	0.217	0.347	M	0.185	M	0.277	0.350	0.402	M	M	0.233	0.368	M	0.179
	II	0.888	1.588	1.583	1.292	1.277	0.678	1.687	1.699	1.397	1.403	0.371	0.549	1.456	1.97	1.247
VAsSe ₃	I	M	HM	0.338	1.635	0.246	M	0.150	0.355	0.344	M	M	0.239	0.428	0.108	M
	II	M	1.301	1.665	0.106	0.251	0.646	1.260	1.565	1.555	0.111	0.385	0.484	1.335	1.017	0.769
VATe ₃	I	M	HM	0.350	M	M	M	0.093	0.203	M	M	0.696	0.217	0.300	M	M
	II	0.708	HM	M	M	M	0.468	M	M	M	M	0.173	M	M	M	M
CrAS ₃	I	0.038	1.221	1.602	1.082	1.001	0.103	1.169	1.456	0.947	0.974	M	0.598	0.855	1.174	0.757
	II	0.273	0.989	1.226	0.865	0.701	0.074	1.069	1.313	1.311	0.793	M	0.550	0.861	1.047	0.950
CrAsSe ₃	I	M	1.066	1.234	1.010	0.839	0.021	0.879	1.135	1.115	0.703	M	0.674	0.941	0.823	0.406
	II	0.157	0.536	0.890	0.937	0.454	0.181	0.531	0.799	0.859	0.427	0.316	0.470	0.654	0.505	0.432
CrATe ₃	I	M	0.645	0.776	0.378	0.817	0.118	0.421	0.705	0.432	0.270	M	0.527	0.545	M	M
	II	M	0.155	0.455	0.624	0.106	M	0.034	0.169	0.529	M	M	0.112	0.178	0.365	M
MnAS ₃	I	M	HM	0.101	0.082	M	M	M	M	0.101	M	M	M	M	0.014	M
	II	1.206	HM	SM	0.372	M	1.242	HM	M	M	0.108	M	HM	0.555	M	M
MnAsSe ₃	I	M	HM	M	M	M	M	M	M	M	M	0.055	M	M	M	0.244
	II	0.822	HM	M	M	M	0.233	HM	M	M	M	M	HM	M	M	M
MnATe ₃	I	M	HM	M	M	M	M	M	M	M	M	M	M	M	M	M
	II	0.278	HM	M	M	M	M	HM	M	M	M	M	HM	M	M	M
FeAS ₃	I	0.266	HM	M	0.486	0.074	0.099	1.028	0.129	0.785	0.730	M	HM	M	0.487	0.510
	II	M	M	0.591	0.729	M	1.006	0.716	0.569	0.730	0.089	1.242	HM	0.315	0.287	0.090
FeAsSe ₃	I	0.298	M	M	0.703	0.514	0.180	HM	M	0.622	0.486	M	HM	M	0.433	0.406
	II	0.717	HM	0.455	0.655	M	0.605	M	0.391	0.567	M	0.982	M	M	M	M
FeATe ₃	I	0.080	0.642	M	0.487	0.378	M	M	M	0.433	0.310	M	M	M	0.208	0.101
	II	M	HM	0.233	0.346	M	M	M	0.162	0.333	M	0.351	M	0.166	M	M
CoAS ₃	I	0.899	–	–	–	–	0.706	–	–	–	–	M	–	–	–	–
	II	1.259	1.259	0.428	M	M	1.061	1.060	M	M	M	0.302	HM	1.014	0.505	M
CoAsSe ₃	I	0.865	–	–	–	–	0.722	–	–	–	–	0.167	–	–	–	–
	II	0.878	0.472	0.683	0.110	M	0.770	0.599	0.770	0.306	0.110	0.466	M	0.417	0.466	0.101
CoATe ₃	I	0.550	–	–	–	–	0.383	–	–	–	–	0.172	–	–	–	–
	II	0.552	0.555	0.555	0.211	M	0.404	0.409	0.299	0.165	M	0.246	M	M	M	M
NiAS ₃	I	M	HM	M	–	0.063	M	–	–	–	–	M	–	–	–	–
	II	M	0.032	SM	M	M	M	HM	M	M	M	M	M	M	M	M
NiAsSe ₃	I	M	HM	M	–	M	M	HM	M	M	–	M	–	–	–	–
	II	M	M	M	M	M	M	HM	M	M	M	M	HM	M	M	M
NiATe ₃	I	M	M	M	–	M	M	M	–	–	–	M	–	–	–	–
	II	M	M	M	M	M	M	M	–	–	–	M	M	–	–	–

be ignored. For example, in the case of the vanadium atom with five valence electrons, two from $4s$ and three from $3d$ atomic orbitals, it is finally left with two unpaired $3d$ electrons leading to $2 \mu_B$ in the 3^+ cation configuration. Following this reasoning, the magnetization increases as we move to the right in the periodic table until it reaches a maximum for Mn^{3+} with four Bohr magnetons. The drop in magnetization to one Bohr magneton for Fe^{3+} may be attributed to changes in the level ordering such that the five $3d$ electrons arrange into three and two electrons with opposing spin alignments. If crystal

field splitting is large, we should expect strongest magnetism when the t_{2g} levels are half-filled or when the e_g levels are half-filled, i.e., around d^3 and d^8 . For example, for 3^+ cations, Cr is in d^3 state exhibiting magnetism, whereas Co in d^6 is expected to have its magnetism suppressed when crystal field effects are strong. The small departures in the numerical magnetic moments from the integer values may be attributed to the metallicity of the electronic structure that allows for noninteger magnetic moments and to the partial hybridization of the d electrons of the transition metals with the surrounding

chalcogens and bridge A atoms which makes the crystal-field interpretation for the transition metal bands less accurate.

The critical Néel or Curie temperatures T_c for magnetic ordering were obtained from the diverging point of the heat capacity $C = (\langle E^2 \rangle - \langle E \rangle^2)/(kT^2)$ versus temperature, where k is the Boltzmann constant. We have used the METROPOLIS Monte Carlo simulations of Ising models in periodic lattices of up to 50×50 sites in size [101–103]. The numerical results for the heat capacity as a function of temperature that we used to extract the critical temperatures are presented in Fig. S17 in Ref. [99]. The critical temperatures T_c of the Ising model listed in Table II should be considered upper bounds for the Heisenberg Hamiltonians when their anisotropy energy is very large. Therefore it is expected that the actual critical temperatures are generally substantially smaller.

We have further compared our results against the anisotropic Heisenberg model whose total energy per metal atom reads

$$H = -\frac{1}{2N_{\text{cell}}} \sum_{i,j} J_{ij} (S_i^z S_j^z + S_i^x S_j^x + S_i^y S_j^y) + E_{\text{ani}}(\theta), \quad (5)$$

where $E_{\text{ani}}(\theta)$ is the total energy difference between the easy axis to all possible spin directions θ where N_{cell} is the total number of metal atoms in the supercell. We assumed $E_{\text{ani}}(\theta, \phi) \simeq E_{\text{ani}}(\theta)$ neglecting the weak ϕ dependence in the x - y plane. The scan of total energies for all spin directions is done by performing calculations based on fully relativistic pseudopotentials on top of atomic coordinates obtained relaxing with scalar relativistic pseudopotentials [104,105]. We define the magnetocrystalline anisotropy energy (MAE) as the difference of total energy between two spin directions calculated for the easy and hard axes

$$\text{MAE} = \max(E_{\text{ani}}(\theta)) \quad (6)$$

that by definition will be a positive number. We list in Table I the magnetic anisotropy energies (MAE) calculated for the FM and nAFM phases. These energies are obtained by first relaxing the ground states within scalar-relativistic spin collinear calculations, and then orienting the spin directions within the fully relativistic spin noncollinear calculations [105]. The $E_{\text{ani}}(\theta)$ can be fitted by

$$E_{\text{ani}}(\theta) \cong \sum_{n=0}^n a_n \cos(n\omega\theta) + \sum_{n=1}^n b_n \sin(n\omega\theta), \quad (7)$$

where the fitting coefficients (ω, a_n, b_n) are listed in Tables V and VI [99]. An excellent fit is obtained using a few terms in the expansion although in certain cases we have used up to $N = 8$ for an accurate fit. The plots for the $E_{\text{ani}}(\theta)$ is presented in Figs. S15 and S16 [99].

The calculated average values of the magnetic moments at the metal sites vary widely depending on which metal atom we are considering, whereas the numerical averages of the magnetic moments for different magnetic configurations of the same compound have usually smaller differences (between 3%–10%), see Table I. The extracted critical temperatures T_c of Heisenberg model listed in Table II, and the heat capacity plots are presented in Fig. S18 [99]. The Heisenberg Monte Carlo calculations follow a recipe outlined in Ref. [106] and explained in Refs. [102,103]. The lattice sites with 50×50

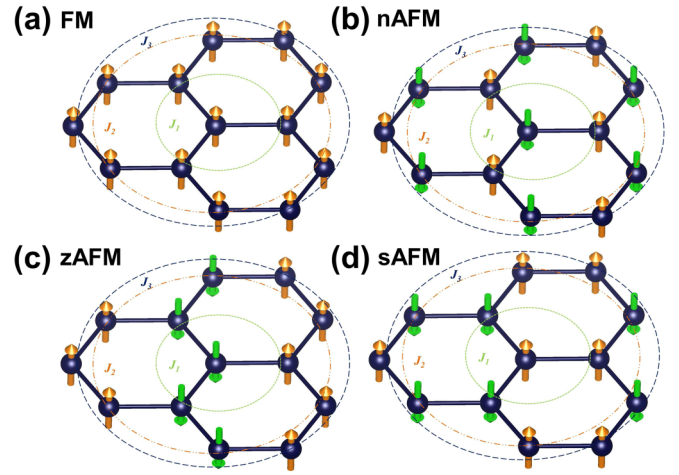


FIG. 4. Schematic representations of different magnetic configurations in a honeycomb lattice of transition metal atoms where the magnetic moments are primarily located. We can classify the phases as (a) ferromagnetic, (b) Néel antiferromagnetic, (c) zigzag antiferromagnetic, and (d) stripy antiferromagnetic. The exchange coupling constants J_1 , J_2 , and J_3 represent respectively the first, second, and third nearest neighbors of the central atom site that are indicated by the green (short dashes), the orange (dash-dotted), and navy blue (dashed) lines.

with brick lattice configurations used to perform the Monte Carlo calculations in honeycomb lattice in both the Ising and Heisenberg calculations. Total 200 000 Monte Carlo steps were used, among them 100 000 step for each thermalization and for averaging the observables.

C. Electronic structure and density of states

We now turn our attention to the electronic band structure and density of states that dictate the electronic properties of these materials. In particular it is desirable to understand the interdependence between electronic structure and the magnetic configuration to explore applications that couple the spin and charge degrees of freedom in transport or optical experiments. The electronic structure of MAX_3 materials were obtained within DFT+D2 and DFT+D2+ U , and among the materials studied there are both ferromagnets and antiferromagnets, and both metals and insulators. See Table III for a list of the different solutions. We have loosely classified as semimetallic those states with vanishingly small gaps or small density of states (DOS) near the Fermi energy from inspection of the electronic structure. The electronic band structures for the ground-state configurations are shown in Fig. 5 and the corresponding DOS can be found in Fig. 6 for DFT-D2 (see Ref. [99] for band structures and the corresponding DOS for DFT-D2+ U as Figs. S2 and S3).

The band structure plots have used a triangular unit cell around one of the K valleys, while we doubled the cell size to allow for longer period zAFM and sAFM magnetic configurations. The DOS for all magnetic (FM, nAFM, zAFM, and sAFM) and nonmagnetic phases within DFT-D2 and DFT-D2+ U as well as the analysis of the orbital projected partial density of states in Figs. S4 to S12 [99] reveals that the conduction or valence band edges have an important

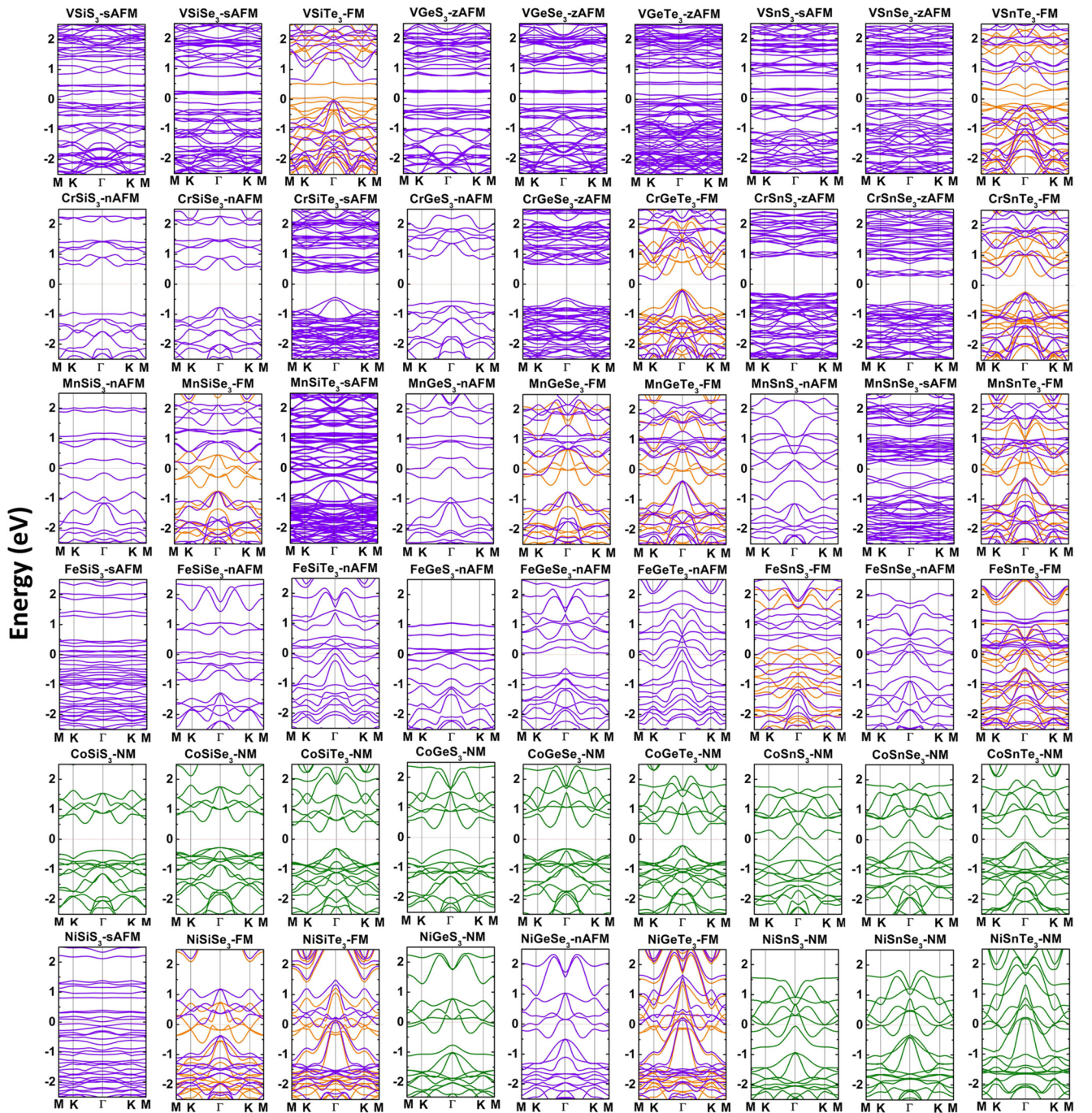


FIG. 5. DFT-D2 band structures for single-layer MAX_3 compounds in their lowest-energy magnetic configurations for $M = V$, Cr, Mn, Fe, Co and Ni transition-metal atoms combined with $A = Si, Ge, Sn$ group IV and $X = S, Se, Te$ chalcogen atoms. The plotted band structures were calculated using the triangular structural unit cell, except for the cases of sAFM and zAFM that have a larger periodicity in the magnetic structure. There we used a triangular unit cell with doubled lattice constant. The bands are violet for AFM configurations, violet and orange for the up and down split spin bands in the FM configurations, and green for the NM phases. The Fermi energy is positioned at $E = 0$.

contribution from the d orbitals of metal atoms as well as s and p orbitals of the A and X atoms.

The k -point resolved orbital projected density of states for the specific case of $CrGeTe_3$ shown in Fig. 7 allows to visualize the orbital contributions from all three atoms and the degree of their hybridization for the states near the valence and conduction band edges. The differences in the density of state

profiles between DFT+D2 and DFT+D2+ U calculations indicate that the electronic structures depend sensitively on the choice of electron-electron interaction model which tend to split further the d -orbital bands. As expected, most of the AFM configurations are found to be semiconductors while semimetallic and metallic solutions are also found for select spin configurations in V and Cr tellurides, in two instances

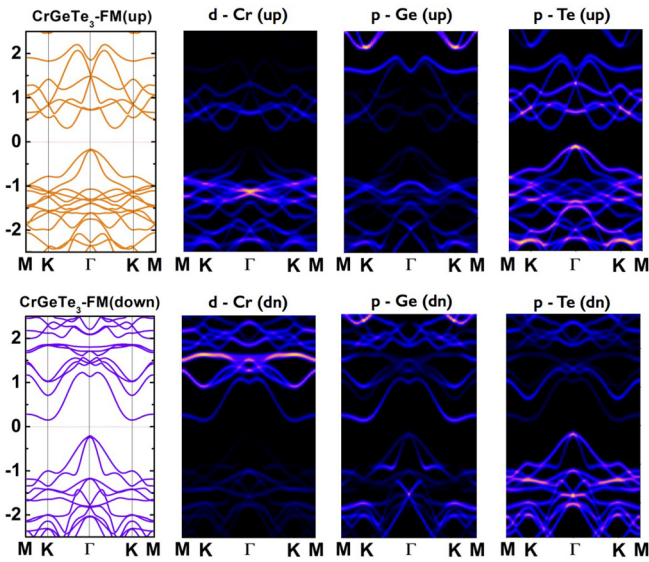


FIG. 7. Representation of the band structure and k -point resolved orbital projected density of states for up and down spin configurations of FM-CrGeTe₃. The plots for the content of d orbital for Cr and the p orbital for Ge and Te atoms reveal that contributions from all three atoms are present for the states near the valence and conduction band edges.

of Mn sulfides, and in several Fe based compounds, see Fig. 5. As a general behavior, for both AFM as well as NM configurations the band gaps reduce when the chalcogen's atomic number increases from S to Te. The FM configurations are generally metallic, with half metallic solutions for VSiTe₃, MnSiSe₃, FeSnS₃, NiSiSe₃, and semiconducting solutions for CrGeTe₃, FeSnS₃, and FeSnTe₃. We notice that the addition of U switches some of the metallic FM solutions into half-metals, and it leads to semiconducting FM solutions for CrSnS₃, CrSnSe₃, and CoSnS₃. Most of the Co based compounds predict NM states with a semiconducting gap, while the few NM states of Ni based compounds are found to be metallic. The density of states (DOS) presented in Fig. 6 undergo notable changes when the Coulomb correlations are accounted for through the parameter U , indicating that correlations can dominate the magnetic properties in MAX₃ compounds. Therefore the modeling of these magnetic materials can benefit from experimental input or higher level *ab initio* calculations. The analysis from the projected density of states (PDOS) for the orbital content of the valence and conduction band edges provide information that is relevant for studies of carrier-density dependent magnetic properties. Depending on the specific material composition and magnetic configuration, the valence and conduction band edge orbitals are dominated by metal, nonmetal or chalcogen atoms. We expect greater sensitivity of MAX₃ layers at contact with charge polarized interfaces when the electrons at the band edge are predominantly distributed at the chalcogens.

IV. CARRIER AND STRAIN TUNABLE MAGNETISM

As we reported in the case of MPX₃ layered compounds [54], the possibility of altering the properties of

2D magnetic materials by means of experimentally tunable parameters make these materials promising for a host of spintronics applications. The main two control knobs that we explore in this section are the carrier density and strains. Carrier density doping can be envisioned through field effects in transistor setups or by forming interfaces with charge polarized ferroelectric materials or ionic molecules. If magnetic transitions can be achieved with carrier densities accessible in conventional transistors they would provide a convenient route for electrical manipulation of magnetic properties. Likewise, the strains generated by mechanical bending, pressure or stretching of 2D materials would pave the way towards piezomagnetic control.

A. Field-effect control of magnetic properties

The possibility of controlling the magnetic properties of a device through a gate voltage offers advantages over magnetic-field mediated control in terms of speed and spatial resolution. If achieved using 2D material devices they would have an additional advantage of further reduced energy cost per device operation compared to conventional devices. Control of magnetic order through electric fields have been achieved in ferromagnetic semiconductors and in metal films where the magnetic exchange coupling and the magnetic anisotropy can be tuned by modifying the position of the Fermi level [107–109]. A schematic illustration for a field effect transistor device where magnetic order is modified through a carrier inducing backgate is shown in Fig. 8 for DFT-D2 (see Ref. [99] for using DFT-D2+ U method as Fig. S12). In this same figure we summarize our results for the theoretically predicted trends for the competition between AFM and FM states for 2D MAX₃ compounds that we have considered. In our calculations, we have obtained the variation of the total energy differences between magnetic configurations as a function of carrier density neglecting the effects of carrier inhomogeneity within the layer due to the presence of external electric fields. When the ground state is in the AFM phase it is often possible to trigger a transition to FM phases when we include a sufficiently large electron or hole carrier densities. This behavior can be understood intuitively when FM phases are gapless or have smaller gaps than the AFM phases [54]. By defining the gap difference $\Delta E^{\text{gap}} = E_{\text{AFM}}^{\text{gap}} - E_{\text{FM}}^{\text{gap}}$ between the gap in the AFM phase and the FM phases, it follows that the total energy difference $\delta E \equiv E_{\text{AFM}} - E_{\text{FM}}$ per unit area can be written as

$$\delta E(\pm\delta n) = \delta E_0 + (\Delta E^{\text{gap}}/2 \pm \delta\mu)(\pm\delta n), \quad (8)$$

where the carrier density of n -type samples is $+\delta n$, the density for p -type samples is $-\delta n$, the energy difference between AFM and FM phases in neutral MAX₃ sheets is given by δE_0 , and the difference between the mid-gap energy in the AFM semiconductors and the chemical potential of the ferromagnetic phase is $\delta\mu$. Therefore, for positive (negative), $\delta\mu$ the transition from AFM to FM phase is most effective for electron doping (hole doping). We show in Fig. S13 in Ref. [99] the total DOS corresponding to FM and AFM phases of CrSiTe₃ in the presence of carrier doping as a specific example, while a detailed breakdown of the projected density of states at each atomic site as a function of carrier density

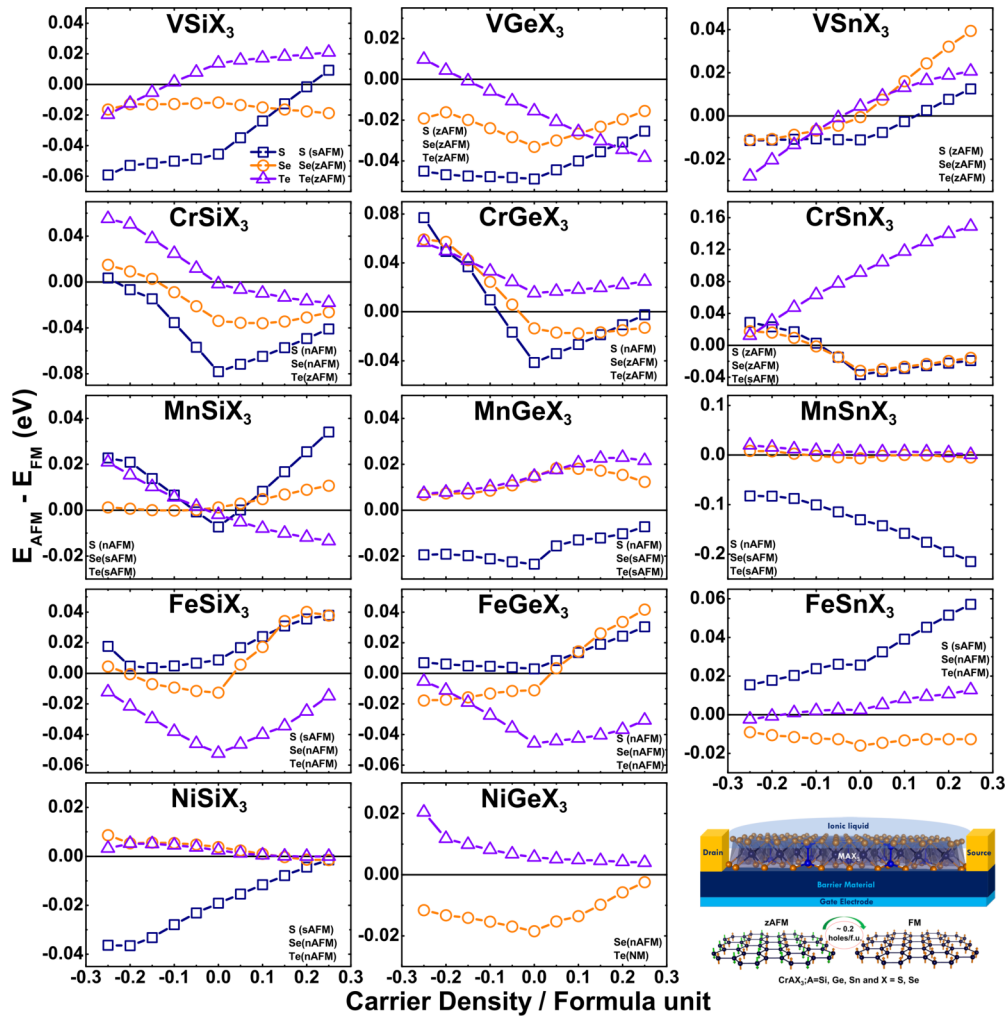


FIG. 8. Carrier density dependent total energy differences per MAX_3 formula unit between the AFM and FM phases of V, Cr, Mn, Fe, Ni based single-layer trichalcogenides obtained within DFT-D2. The AFM ground-states favored near charge neutrality can often be switched to FM phases either for electron or hole doping for sufficiently large carrier densities in V, Mn, Ni, and Fe based compounds. Cusps in the total energy differences are seen near charge neutrality in gapped AFM materials manifesting the transition from electron to hole doping. Carrier densities of up to a few $\sim 10^{14}$ electrons per cm^2 should be in principle accessible through ionic liquid or gel gating. A carrier density of 0.1 electrons per MAX_3 formula unit corresponds to $\sim 6 \times 10^{13}$ electrons per cm^2 when the distance between the metal atoms is ~ 6 Å. We label within brackets the expected phase, i.e., nonmagnetic (NM), Néel antiferromagnetic (nAFM), zigzag antiferromagnetic (zAFM) and stripy antiferromagnetic (sAFM) that transition from ferromagnetic (FM) state next to each compound.

can be found in Fig. S13 in Ref. [99]. It is expected that the transition between AFM and FM phases can happen for relatively small total carrier density modification when the total energy difference per formula unit is smaller than the band gap. We can see in Fig. 8 that magnetic phase transitions are expected in $CrSiTe_3$, $MnSiX_3$, and $CrGeSe_3$ at electron carrier densities and $MnSiS_3$, $FeSiSe_3$, $FeGeSe_3$, and $VSnSe_3$ at hole densities as small as ~ 0.05 electrons per formula unit which correspond to carrier densities on the order of $\sim 10^{13} cm^{-2}$. Carrier densities of this magnitude could be achievable in field effect transistor devices or by gating with ionic liquids. However, cases like vanadium based $VSiSe_3$, $VGeS_3$, $VGeSe_3$, or iron based $FeSiTe_3$, $FeSnS_3$, $FeSnSe_3$, or manganese based $MnGeX_3$, $MnSnS_3$, or $NiGeX_3$, $CrSnTe_3$, have not shown any transition within the selected range of electron or hole carrier density. For compounds whose

ground-states are FM at charge neutrality we find that the transitions to the AFM phase can be achieved for n doping in $VSiTe_3$, $VSnTe_3$, $MnSiSe_3$, and $FeSnTe_3$ and for p doping for $NiSiSe_3$, $NiSTe_3$, and $MnSnTe_3$. The use of appropriate contacts in transport devices can facilitate the preparation of n or p carrier doped samples by aligning the Fermi level towards the conduction or valence band edges.

B. Strain-tunable magnetic properties

Ultrathin 2D materials lie at the frontier between soft and hard condensed matter thanks to their membranelike flexibility which has led to proposals that engineer their electronic properties by means of strains. Taking graphene as an example, the appropriate generation of strains could lead to large pseudomagnetic fields [110], or cause the generation

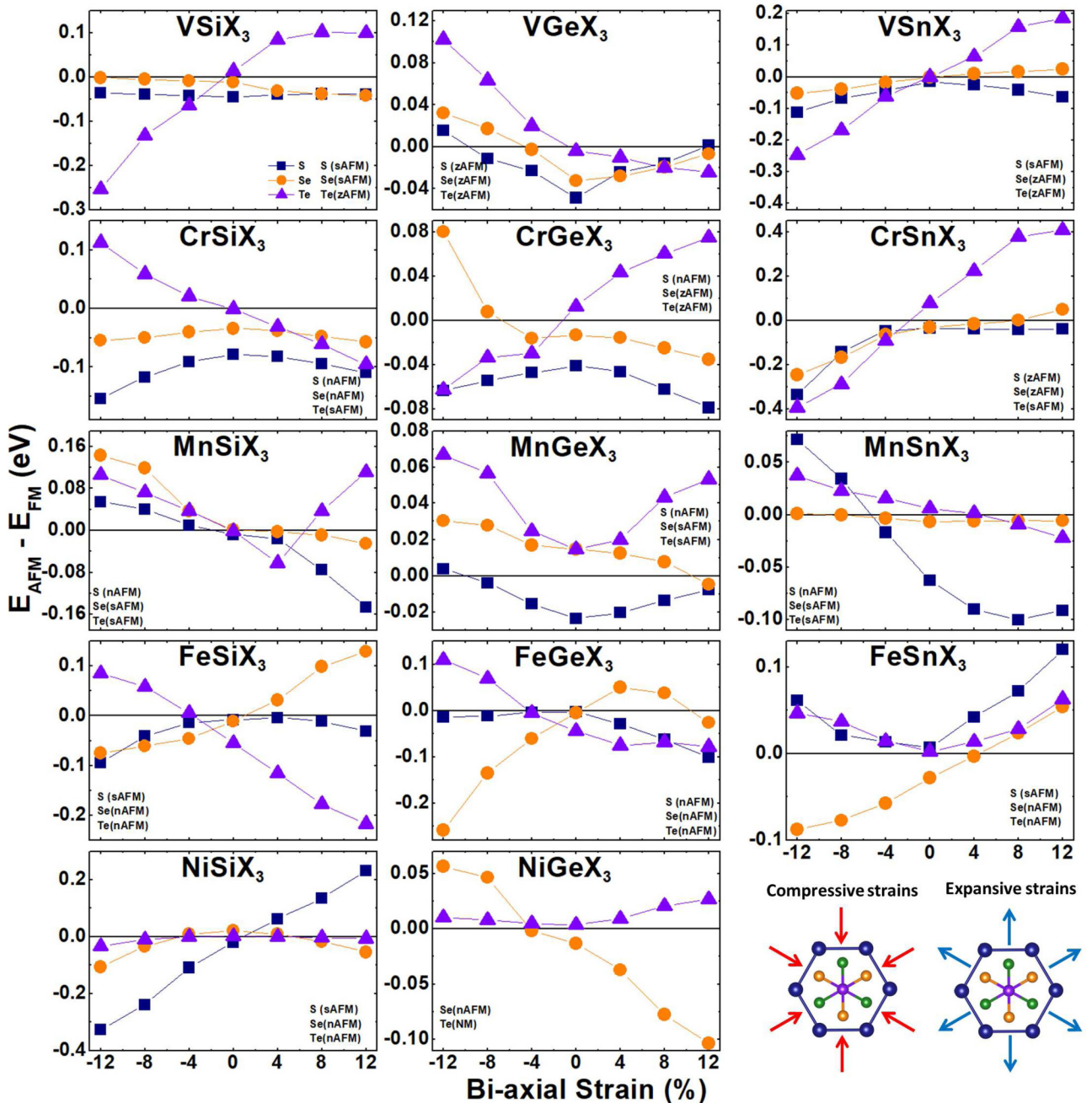


FIG. 9. Influence of in-plane strain on the magnetic configurations of selected MAX_3 compounds. Magnetic phase transitions are introduced by in-plane biaxial compressive and expansive strains for several magnetic MAX_3 compounds at zero carrier density. We notice that the magnetic phase energy differences in some compounds are especially susceptible to the strains suggesting that large variations in T_c values may be achievable by strain engineering. We indicate next to each chalcogen atom label the magnetic configuration to which the FM phase transitions.

of primary Dirac point band gaps in nearly aligned graphene on hexagonal boron nitride [111–114]. In order to assess the role of strains in the electronic structure of ultrathin 2D MAX_3 materials we calculate the total energies of the different magnetic phases in the presence of expansive or compressive in-plane biaxial strains that we model by uniformly scaling the rectangular unit cell, see Fig. 9. The uniform biaxial strains lead to modifications in the magnetic phase energy differences $E_{AFM} - E_{FM}$ that can trigger phase transitions for strains as small as 2%–4% in certain cases, while much larger strain

fields are required in general. In the following, we list the five different types of strain-induced effects expected in charge neutral MAX_3 compounds.

(1) No phase change (expansion and compression). The ground states are not altered in the presence of strains for vanadium based $VSiS_3$ (sAFM), $VSnS_3$ (zAFM), chromium based $CrSiS_3$ (nAFM), $CrSiSe_3$ (nAFM), $CrGeS_3$ (nAFM), $CrSnS_3$ (zAFM), manganese based $MnGeTe_3$ (FM), iron based $FeSnS_3$ (FM), $FeSnTe_3$ (FM), and nickel based $NiGeTe_3$ (FM).

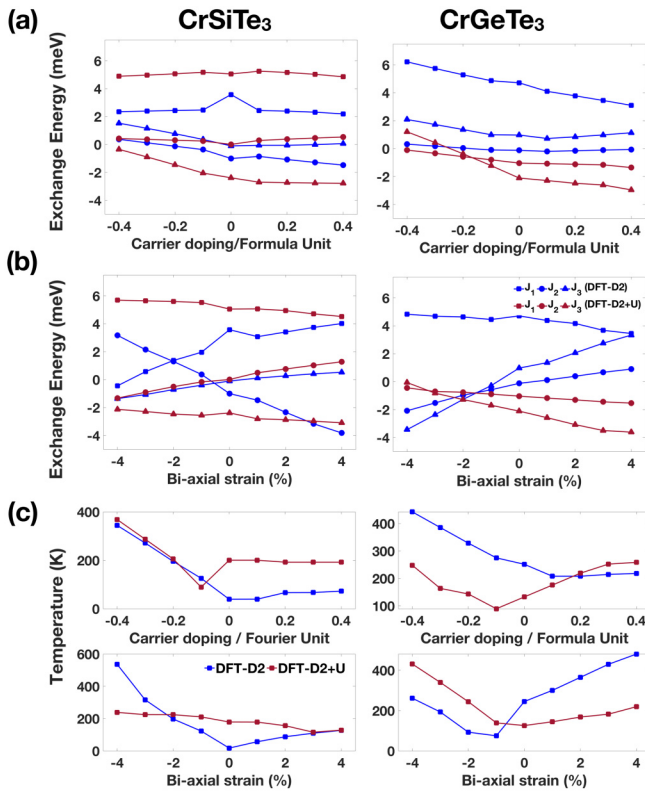


FIG. 10. The evolution of the three nearest-neighbor exchange coupling J parameters as a function of (a) carrier doping per formula unit and (b) biaxial strain imposed by modifying the dimensions of the rectangular unit cell. (c) The variation of critical temperature as a function of carrier doping (top) and biaxial (bottom) strain in CrSiTe₃ (left) and CrGeTe₃ (right), calculated within DFT-D2 and DFT-D2+ U .

(2) AFM to FM (compression). For compressive strains we find transitions for vanadium based VSiSe₃ (4%), VGeS₃ (~1%), VGeSe₃ (4%), VGeTe₃ (9%), chromium based CrSiTe₃ (~1%), CrGeTe₃ (7%), manganese based MnSiS₃ (2%), MnSiTe₃ (~1%), MnGeS₃ (9%), MnSnS₃ (4%), MnSnSe₃ (8%), iron based FeSiTe₃ (4%), FeGeTe₃ (4%), and nickel based NiGeSe₃ (4%).

(3) AFM to FM (expansion). Conversely for expansive strains we find transitions in vanadium based VGeS₃ (~12%), VSnSe₃ (~2%) chromium based CrSiTe₃ (~2%), CrSnSe₃ (8%), manganese based MnSiTe₃ (~6%), iron based FeSiSe₃ (1%), FeGeSe₃ (1%), FeSnSe₃ (4%), and nickel based NiSiS₃ (1%).

(4) FM to AFM (compression). Transitions are seen for compressive strains (%) in vanadium based VSiTe₃ (~1%), VSnTe₃ (~1%), chromium based CrGeTe₃ (~2%), CrSnTe₃ (~2%), iron based FeSiS₃ (1%) and, nickel based NiSiSe₃ (4%), NiSiTe₃ (4%).

(5) FM to AFM (expansion): Transitions for expansive strains (%) are found for manganese based MnSiSe₃ (~1%), MnSnTe₃ (4%), iron based FeSiS₃ (4%), and nickel based NiSiSe₃ (4%), NiSiTe₃ (4%).

An example about the DOS evolution as a function of strain is shown in Fig. S14 in Ref. [99] for charge neutral CrSiTe₃ monolayer subjected to -4% (compressive)

and 4% (expansive) strains in the FM and zAFM phases. The expansion strains are found to have a small effect in both the FM and zAFM phases of CrSiTe₃ but compressive strains of 4% lead to a closure of the FM-CrSiTe₃ band gap turning it into a semimetal with a small finite density of states at the Fermi level. As mentioned earlier, from the projected density of states analysis in Fig. S14 in Ref. [99], we can observe a relatively large content of Cr- d and Si- s, p orbitals at the bands near the Fermi energy.

Figure 10(c) illustrates how the T_c can be modified by carrier density variations or strains that can be applied in the system by gating or compression/expansion of the sample see Figs. 10(a) and 10(b) for J parameters comparison as function of strain and carrier doping as Table IV in Ref. [99]. For monolayer CrSiTe₃, we showed that substantial increases of the T_c can be achieved for large hole doping and compressive strains.

V. SUMMARY AND CONCLUSIONS

In this work, we have presented an *ab initio* study for the electronic and magnetic properties of single-layer MAX₃ transition metal trichalcogenide materials composed by 3d transition metal ($M = V, Cr, Mn, Fe, Co, Ni$), group IV elements ($A = Si, Ge, Sn$) and chalcogen ($X = S, Se, Te$) atoms. Our DFT calculations indicate that a variety of magnetic ground states are supported depending on material composition, including AFM phases in either Néel, stripy, zigzag configurations, as well as FM configurations. The various magnetic phases including FM, AFM and nonmagnetic (NM) phases are found to exist for both metallic and semiconducting states indicating the large pool of material combinations possible for prospective applications in devices. The specific choice of the unit cell either triangular or rectangular as well and the supercell dimension impact the total energy of the ground states for the different magnetic phases which indicates the sensitivity of the magnetic ground-state solutions to the geometry of the chemical bonds. Compounds such as CoAX₃ and NiAX₃ are nonmagnetic within semilocal DFT-D2, although they can stabilize magnetic phases upon inclusion of a sufficiently large U at the metal atom sites. The important differences in the predicted results obtained within DFT-D2 and those obtained including a local U correction indicate the importance of correctly capturing the Coulomb correlation effects and calls for further experimental search of this class of material compounds to combine the results with the theoretical modeling of the exchange interactions. We have analyzed the stability of the magnetic phases on the Ising model of a honeycomb lattice where the exchange coupling parameters are obtained from the total energy differences corresponding to different metastable spin configurations. This approach is expected to be valid for insulating phases with localized electrons and when the magnetic anisotropies are large. The critical temperatures that we obtained within the same unified Metropolis statistical analysis framework [102] should be seen as an upper bound for the expected critical temperatures of a classical Heisenberg model with magnetic anisotropy. We have then obtained the magnetic phase diagram map as a function of carrier density

and strains which should be parameters that are controllable in experiments. The devices based on 2D materials are particularly suited for field effect control of carrier density which can be enhanced by using high- κ dielectrics, ionic liquids, or by interfacing with ferroelectric materials. We have also explored the possibility of modifying the magnetic phases by means of strains and found that the ground state magnetic configuration can undergo phase transitions driven by in-plane compression or expansion of the lattice constants as small as a few percents in certain cases. Our study suggests that the large variety of available material compositions of single-layer MAX_3 transition metal trichalcogenides and the possibility of controlling environment parameters such as carrier density and strains in experiments makes these materials promising for 2D spintronics research. These control knobs can be useful not only for triggering magnetic phase

transitions but for enhancing the critical temperatures of the magnetic phases to make the devices more useful in practical applications.

ACKNOWLEDGMENTS

Computations were carried out using the resources provided by the Texas Advanced Computing Centre (TACC). This project was supported financially by NRF-2017R1D1A1B03035932 and by the Basic Science Research Program through the National Research Foundation of Korea (NRF) funded by the Ministry of Education (2018R1A6A1A06024977) for B.L.C., DOE Grant No. FG02-02ER45958, and Welch Foundation Grant No. TBF1473 for A.H.M., and NRF-2017R1A2A2A05001403 for E.H.H., and by the 2017 Research Fund of the University of Seoul for J.J.

- [1] K. S. Novoselov, A. K. Geim, S. V. Morozov, D. Jiang, M. I. Katsnelson, I. V. Grigorieva, S. V. Dubonos, and A. A. Firsov, Two-dimensional gas of massless Dirac fermions in graphene, *Nature (London)* **438**, 197 (2005).
- [2] Y. Zhang, Y.-W. Tan, H. L. Stormer, and P. Kim, Experimental observation of the quantum Hall effect and Berry's phase in graphene, *Nature (London)* **438**, 201 (2005).
- [3] K. S. Novoselov, D. Jiang, F. Schedin, T. J. Booth, V. V. Khotkevich, S. V. Morozov, and A. K. Geim, Two-dimensional atomic crystals, *Proc. Natl. Acad. Sci. USA* **102**, 10451 (2004).
- [4] M. Chhowalla, H. S. Shin, G. Eda, L.-J. Li, K. P. Loh, and H. Zhang, The chemistry of two-dimensional layered transition metal dichalcogenide nanosheets, *Nat. Chem.* **5**, 263 (2013).
- [5] L. Britnell, R. M. Ribeiro, A. Eckmann, R. Jalil, B. D. Belle, A. Mishchenko, Y.-J. Kim, R. V. Gorbachev, T. Georgiou, S. V. Morozov, A. N. Grigorenko, A. K. Geim, C. Casiraghi, A. H. Castro Neto, and K. S. Novoselov, Strong light-matter interactions in heterostructures of atomically thin films, *Science* **340**, 1311 (2013).
- [6] B. Burk, R. E. Thomson, J. Clarke, and A. Zettl, Surface and bulk charge density wave structure in 1 T-TaS₂, *Science* **257**, 362 (1992).
- [7] A. H. Castro Neto, Charge Density Wave, Superconductivity, and Anomalous Metallic Behavior in 2D Transition Metal Dichalcogenides, *Phys. Rev. Lett.* **86**, 4382 (2001).
- [8] R. F. Frindt, Superconductivity in Ultrathin NbSe₂ Layers, *Phys. Rev. Lett.* **28**, 299 (1972).
- [9] D. Costanzo, S. Jo, H. Berger, and A. F. Morpurgo, Gate-induced superconductivity in atomically thin MoS₂ crystals, *Nat. Nanotech.* **11**, 339 (2016).
- [10] J.-U. Lee, S. Lee, J. H. Ryoo, S. Kang, T. Y. Kim, P. Kim, C.-H. Park, J.-G. Park, and H. Cheong, Ising-type magnetic ordering in atomically thin FePS₃, *Nano. Lett.* **16**, 7433 (2016).
- [11] K.-z. Du, X.-z. Wang, Y. Liu, P. Hu, M. I. B. Utama, C. K. Gan, Q. Xiong, and C. Kloc, Weak van der Waals stacking, wide-range band gap, and Raman study on ultrathin layers of metal phosphorus trichalcogenides, *Nano. Lett.* **10**, 1738 (2016).
- [12] X. Wang, K. Du, Y. Y. F. Liu, P. Hu, J. Zhang, Q. Zhang, M. H. S. Owen, X. Lu, C. K. Gan, P. Sengupta, C. Kloc, and Q. Xiong, Raman spectroscopy of atomically thin two-dimensional magnetic iron phosphorus trisulfide (FePS₃) crystals, *2D Mater.* **3**, 031009 (2016).
- [13] S. Lee, K. Choi, S. Lee, B. H. Park, and J. Park, Tunneling transport of mono- and few-layers magnetic van der Waals MnPS₃, *APL Mater.* **4**, 086108 (2016).
- [14] M.-W. Lin, H. L. Zhuang, J. Yan, T. Z. Ward, A. A. Puzos, C. M. Rouleau, Z. Gai, L. Liang, V. Meunier, B. G. Sumpter, P. Ganesh, P. R. C. Kent, D. B. Geohegan, D. G. Mandrus, and K. Xiao, Ultrathin nanosheets of CrSiTe₃: A semiconducting two-dimensional ferromagnetic material, *J. Mater. Chem. C* **4**, 315 (2016).
- [15] B. Huang, G. Clark, E. Navarro-Moratalla, D. R. Klein, R. Cheng, K. L. Seyler, D. Zhong, E. Schmidgall, M. A. McGuire, D. H. Cobden, W. Yao, D. Xiao, P. Jarillo-Herrero, and X. Xu, Layer-dependent ferromagnetism in a van der Waals crystal down to the monolayer limit, *Nature (London)* **546**, 270 (2017).
- [16] C. Gong, L. Li, Z. Li, H. Ji, A. Stern, Y. Xia, T. Cao, W. Bao, C. Wang, Y. Wang, Z. Q. Qiu, R. J. Cava, S. G. Louie, J. Xie, and X. Zhang, Discovery of intrinsic ferromagnetism in two-dimensional van der Waals crystals, *Nature (London)* **546**, 265 (2017).
- [17] C.-T. Kuo, M. Neumann, K. Balamurugan, H. J. Park, S. Kang, H. W. Shiu, J. H. Kang, B. H. Hong, M. Han, T. W. Noh, and J.-G. Park, Exfoliation and Raman spectroscopic fingerprint of few-layer NiPS₃ van der Waals crystals, *Sci. Rep.* **6**, 20904 (2016).
- [18] C.-T. Kuo, K. Balamurugan, H. W. Shiu, H. J. Park, S. Sinn, M. Neumann, M. Han, Y. J. Chang, C.-H. Chen, H.-D. Kim, J.-G. Park, and T. W. Noh, The energy band alignment at the interface between mechanically exfoliated few-layer NiPS₃ nanosheets and ZnO, *Curr. App. Phys.* **16**, 404 (2016).
- [19] W. Xing, Y. Chen, P. M. Odenthal, X. Zhang, W. Yuan, T. Su, Q. Song, T. Wang, J. Zhong, S. Jia, X. C. Xie, Y. Li, and W. Han, Electric field effect in multilayer Cr₂Ge₂Te₆: A ferromagnetic 2D material, *2D Mater.* **4**, 024009 (2017).
- [20] J. Chu, F. Wang, L. Yin, L. Lei, C. Yan, F. Wang, Y. Wen, Z. Wang, C. Jiang, L. Feng, J. Xiong, Y. Li, and J. He, High-performance ultraviolet photodetector based on a few-layered 2D NiPS₃ nanosheet, *Adv. Funct. Mater.* **27**, 1701342 (2017).

- [21] L. D. Casto, A. J. Clune, M. O. Yokosuk, J. L. Musfeldt, T. J. Williams, H. L. Zhuang, M.-W. Lin, K. Xiao, R. G. Hennig, B. C. Sales, J.-Q. Yan, and D. Mandrus, Strong spin-lattice coupling in CrSiTe₃, *APL Mater.* **3**, 041515 (2015).
- [22] T. J. Williams, A. A. Aczel, M. D. Lumsden, S. E. Nagler, M. B. Stone, J.-Q. Yan, and D. Mandrus, Magnetic correlations in the quasi-2d semiconducting ferromagnet CrSiTe₃, *Phys. Rev. B* **92**, 144404 (2015).
- [23] V. Carreaux, D. Brunet, G. Ouvrard, and G. Andre, Crystallographic, magnetic and electronic structures of a new layered ferromagnetic compound Cr₂Ge₂Te₆, *J. Phys: Cond. Mater* **7**, 69 (1995).
- [24] H. Ji, R. A. Stokes, L. D. Alegria, E. C. Blomberg, M. A. Tanatar, A. Reijnders, L. M. Schoop, T. Liang, R. Prozorov, K. S. Burch, N. P. Ong, J. R. Petta, and R. J. Cava, A ferromagnetic insulating substrate for the epitaxial growth of topological insulators, *J. App. Phys.* **114**, 114907 (2013).
- [25] L. D. Alegria, H. Ji, N. Yao, J. J. Clarke, R. J. Cava, and J. R. Petta, Large anomalous Hall effect in ferromagnetic insulator-topological insulator heterostructures, *Appl. Phys. Lett.* **105**, 053512 (2014).
- [26] X. Zhang, Y. Zhao, Q. Song, S. Jia, J. Shi, and W. Han, Magnetic anisotropy of the single-crystalline ferromagnetic insulator Cr₂Ge₂Te₆, *Jpn. J. Appl. Phys.* **55**, 033001 (2016).
- [27] D. Yang, W. Yao, Q. Chen, K. Peng, P. Jiang, X. Lu, C. Uher, T. Yang, G. Wang, and X. Zhou, Cr₂Ge₂Te₆: High thermoelectric performance from layered structure with high symmetry, *Chem. Mater* **28**, 1611 (2016).
- [28] Y. Liu and C. Petrovic, Critical behavior of quasi-two-dimensional semiconducting ferromagnet Cr₂Ge₂Te₆, *Phys. Rev. B* **96**, 054406 (2017).
- [29] Q. L. Pei, X. Luo, G. T. Lin, J. Y. Song, L. Hu, Y. M. Zou, L. Yu, W. Tong, W. H. Song, W. J. Lu, and Y. P. Sun, Spin dynamics, electronic, and thermal transport properties of two-dimensional CrPS₄ single crystal, *J. Appl. Phys.* **119**, 043902 (2016).
- [30] C. C. Mayorga-Martinez, Z. Sofer, D. Sedmidubský, Š. Huber, A. Y. S. Eng, and M. Pumera, Layered metal thiophosphate materials: Magnetic, electrochemical, and electronic properties, *ACS Appl. Mater. Interfaces* **9**, 12563 (2017).
- [31] M. A. McGuire, V. O. Garlea, K. C. Santosh, V. R. Cooper, J. Yan, H. Cao, and B. C. Sales, Antiferromagnetism in the van der Waals layered spin-lozenge semiconductor CrTe₃, *Phys. Rev. B* **95**, 144421 (2017).
- [32] M. A. McGuire, G. Clark, Santosh KC, W. M. Chance, G. E. Jellison, Jr., V. R. Cooper, X. Xu, and B. C. Sales, Magnetic behavior and spin-lattice coupling in cleavable van der Waals layered CrCl₃ crystals, *Phys. Rev. Mater.* **1**, 014001 (2017).
- [33] D. Zhong, K. L. Seyler, X. Linpeng, R. Cheng, N. Sivasdas, B. Huang, E. Schmidgall, T. Taniguchi, K. Watanabe, M. A. McGuire, W. Yao, D. Xiao, K. C. Fu, and X. Xu, Van der Waals engineering of ferromagnetic semiconductor heterostructures for spin and valleytronics, *Sci. Adv.* **3**, e1603113 (2017).
- [34] J. Yang, W. Wang, Y. Liu, H. Du, W. Ning, G. Zheng, C. Jin, Y. Han, N. Wang, Z. Yang, M. Tian, and Y. Zhang, Thickness dependence of the charge-density-wave transition temperature in VSe₂, *Appl. Phys. Lett.* **105**, 063109 (2014).
- [35] X. Sun, T. Yao, Z. Hu, Y. Guo, Q. Liu, S. Wei, and C. Wu, In situ unravelling structural modulation across the charge-density-wave transition in vanadium disulfide, *Phys. Chem. Chem. Phys.* **17**, 13333 (2015).
- [36] J. Du, F. Wang, L. Jin, Z. Quan, Y. Bai, and X. Xu, Enhancement of ferromagnetism in FeTe₂ nanoparticles by Cr doping, *Mater. Lett.* **184**, 261 (2016).
- [37] Y. Shao, S. Song, X. Wu, J. Qi, H. Lu, C. Liu, S. Zhu, Z. Liu, J. Wang, D. Shi, S. Du, Y. Wang, and H.-J. Gao, Epitaxial fabrication of two-dimensional NiSe₂ on Ni(111) substrate, *Appl. Phys. Lett.* **111**, 113107 (2017).
- [38] S. Lebegue, T. Björkman, M. Klintonberg, R. M. Nieminen, and O. Eriksson, Two-Dimensional Materials from Data Filtering and *Ab Initio* Calculations, *Phys. Rev. X* **3**, 031002 (2013).
- [39] B. Liu, Y. Zou, L. Zhang, S. Zhou, Z. Wang, W. Wang, Z. Qu, and Y. Zhang, Critical behavior of the quasi-two-dimensional semiconducting ferromagnet CrSiTe₃, *Sci. Rep.* **6**, 33873 (2016).
- [40] X. Chen, J. Qi, and D. Shi, Strain-engineering of magnetic coupling in two-dimensional magnetic semiconductor CrSiTe₃: Competition of direct exchange interaction and superexchange interaction, *Phys. Lett. A* **379**, 60 (2015).
- [41] B. Siberchicot, S. Jobic, V. Carreaux, P. Gressier, and G. Ouvrard, Band structure calculations of ferromagnetic chromium tellurides CrSiTe₃ and CrGeTe₃, *J. Phys. Chem.* **100**, 5863 (1996).
- [42] N. Sivasdas, M. W. Daniels, R. H. Swendsen, S. Okamoto, and D. Xiao, Magnetic ground state of semiconducting transition-metal trichalcogenide monolayers, *Phys. Rev. B* **91**, 235425 (2015).
- [43] J. Liu, S. Y. Park, K. F. Garrity, and D. Vanderbilt, Flux States and Topological Phases from Spontaneous Time-Reversal Symmetry Breaking in CrSi(Ge)Te₃ -Based Systems, *Phys. Rev. Lett.* **117**, 257201 (2016).
- [44] J. Zhang, B. Zhao, Y. Yao, and Z. Yang, Robust quantum anomalous Hall effect in graphene-based van der Waals heterostructures, *Phys. Rev. B* **92**, 165418 (2015).
- [45] X. Tang, D. Fan, K. Peng, D. Yang, L. Guo, X. Lu, J. Dai, G. Wang, H. Liu, and X. Zhou, Dopant induced impurity bands and carrier concentration control for thermoelectric enhancement in p-type Cr₂Ge₂Te₆, *Chem. Mater* **29**, 7401 (2016).
- [46] G. T. Lin, H. L. Zhuang, X. Luo, B. J. Liu, F. C. Chen, J. Yan, Y. Sun, J. Zhou, W. J. Lu, P. Tong, Z. G. Sheng, Z. Qu, W. H. Song, X. B. Zhu, and Y. P. Sun, Tricritical behavior of the two-dimensional intrinsically ferromagnetic semiconductor CrGeTe₃, *Phys. Rev. B* **95**, 245212 (2017).
- [47] Y. Tian, M. J. Gray, H. Ji, R. J. Cava, and K. S. Burch, Magneto-elastic coupling in a potential ferromagnetic 2D atomic crystal, *2D Mater.* **3**, 025035 (2016).
- [48] H. L. Zhuang, Y. Xie, P. R. C. Kent, and P. Ganesh, Computational discovery of ferromagnetic semiconducting single-layer CrSnTe₃, *Phys. Rev. B* **92**, 035407 (2015).
- [49] R. Brec, Review on structural and chemical properties of transition metal phosphorous trisulfides MPS₃, *Solid State Ionics* **22**, 3 (1986).
- [50] P. A. Joy and S. Vasudevan, Magnetism in the layered transition-metal thiophosphates MPS₃ (M = Mn, Fe, and Ni), *Phys. Rev. B* **46**, 5425 (1992).
- [51] X. Li, X. Wu, and J. Yang, Half-metallicity in MnPSe₃ exfoliated nanosheet with carrier doping, *J. Am. Chem. Soc.* **136**, 11065 (2014).

- [52] X. Li, T. Cao, Q. Niu, J. Shi, and J. Feng, Coupling the valley degree of freedom to antiferromagnetic order, *Proc. Natl. Acad. Sci. USA* **110**, 3738 (2013).
- [53] N. Sivadas, S. Okamoto, and D. Xiao, Gate-Controllable Magneto-optic Kerr Effect in Layered Collinear Antiferromagnets, *Phys. Rev. Lett.* **117**, 267203 (2016).
- [54] B. L. Chittari, Y. Park, D. Lee, M. Han, A. H. MacDonald, E. Hwang, and J. Jung, Electronic and magnetic properties of single-layer MPX_3 metal phosphorous trichalcogenides, *Phys. Rev. B* **94**, 184428 (2016).
- [55] H. L. Zhuang and J. Zhou, Density functional theory study of bulk and single-layer magnetic semiconductor $CrPS_4$, *Phys. Rev. B* **94**, 195307 (2016).
- [56] M. Joe, H. Lee, M. M. Alyörük, J. Lee, S. Y. Kim, C. Lee, and J. H. Lee, A comprehensive study of piezomagnetic response in $CrPS_4$ monolayer: Mechanical, electronic properties and magnetic ordering under strains, *J. Phys: Cond. Matt.* **29**, 405801 (2017).
- [57] Y. Ma, Y. Dai, M. Guo, C. Niu, Y. Zhu, and B. Huang, Evidence of the existence of magnetism in pristine VX_2 monolayers ($X = S, Se$) and their strain-induced tunable magnetic properties, *ACS Nano* **6**, 1695 (2012).
- [58] C. Ataca, H. Sahin, and S. Ciraci, Stable, single-layer MX_2 transition-metal oxides and dichalcogenides in a honeycomb-like structure, *J. Phys. Chem. C* **116**, 8983 (2012).
- [59] H. Zhang, L. Liu, and W. Lau, Dimension-dependent phase transition and magnetic properties of VS_2 , *J. Mat. Chem. A* **1**, 10821 (2013).
- [60] H. L. Zhuang, M. D. Johannes, M. N. Blonsky, and R. G. Hennig, Computational prediction and characterization of single-layer CrS_2 , *Appl. Phys. Lett.* **104**, 022116 (2014).
- [61] M. Kan, S. Adhikari, and Q. Sun, Ferromagnetism in MnX_2 ($X = S, Se$) monolayers, *Phys. Chem. Chem. Phys.* **16**, 4990 (2014).
- [62] A. H. M. A. Wasey, S. Chakrabarty, and G. P. Das, Quantum size effects in layered VX_2 ($X = S, Se$) materials: Manifestation of metal to semimetal or semiconductor transition, *J. Appl. Phys.* **117**, 064313 (2015).
- [63] M. Kan, B. Wang, Y. H. Lee, and Q. Sun, A density functional theory study of the tunable structure, magnetism and metal-insulator phase transition in VS_2 monolayers induced by in-plane biaxial strain, *Nano. Res.* **8**, 1348 (2015).
- [64] X. Ji, K. Xu, C. Chen, B. Zhang, H. Wan, Y. Ruan, L. Miao, and J. Jiang, Different charge-storage mechanisms in disulfide vanadium and vanadium carbide monolayer, *J. Mat. Chem. A* **3**, 9909 (2015).
- [65] H. Zhang, Y. Dai, and L. Liu, Novel monolayer pyrite FeS_2 with atomic-thickness for magnetic devices, *Comp. Mat. Sci.* **101**, 255 (2015).
- [66] H. Y. Lv, W. J. Lu, D. F. Shao, Y. Liu, and Y. P. Sun, Strain-controlled switch between ferromagnetism and antiferromagnetism in 1T- CrX_2 ($X = Se, Te$) monolayers, *Phys. Rev. B* **92**, 214419 (2015).
- [67] D. C. Freitas, R. Weht, A. Sulpice, G. Remenyi, P. Strobel, F. Gay, J. Marcus, and M. Núñez-Regueiro, Ferromagnetism in layered metastable 1T- $CrTe_2$, *J. Phys: Cond. Matter* **27**, 176002 (2015).
- [68] J. Zhang, H. Zheng, R. Han, X. Du, and Y. Yan, Tuning magnetic properties of CrS_2 monolayer by doping transition metal and alkaline-earth atoms, *J. Alloys. Compound* **647**, 75 (2015).
- [69] Y. Yue, Electronic and magnetic properties of monolayer MnS_2 , *Mod. Phys. Lett. B* **30**, 1650419 (2016).
- [70] J. A. Reyes-Retana and F. Cervantes-Sodi, Spin-orbital effects in metaldichalcogenide semiconducting monolayers, *Sci. Rep.* **6**, 24093 (2016).
- [71] H. L. Zhuang and R. G. Hennig, Stability and magnetism of strongly correlated single-layer VS_2 , *Phys. Rev. B* **93**, 054429 (2016).
- [72] E. B. Isaacs and C. A. Marianetti, Electronic correlations in monolayer VS_2 , *Phys. Rev. B* **94**, 035120 (2016).
- [73] H.-R. Fuh, B. Yan, S.-C. Wu, C. Felser, and C.-R. Chang, Metal-insulator transition and the anomalous Hall effect in the layered magnetic materials VS_2 and VSe_2 , *New J. Phys.* **18**, 113038 (2016).
- [74] H. Fuh, C. Chang, Y. Wang, R. F. L. Evans, R. W. Chantrell, and H. Jeng, Newtype single-layer magnetic semiconductor in transition-metal dichalcogenides VX_2 ($X = S, Se$ and Te), *Sci. Rep.* **6**, 32625 (2016).
- [75] H.-R. Fuh, K.-W. Chang, S.-H. Hung, and H.-T. Jeng, Two-dimensional magnetic semiconductors based on transition-metal dichalcogenides VX_2 ($X = S, Se, Te$) and similar layered compounds VI_2 and $Co(OH)_2$, *IEEE. Mag. Lett.* **8**, 3101405 (2016).
- [76] W. Xiong, C. Xia, J. Du, T. Wang, X. Zhao, Y. Peng, Z. Wei, and J. Li, Electrostatic gating dependent multiple-band alignments in a high-temperature ferromagnetic $Mg(OH)_2/VS_2$ heterobilayer, *Phys. Rev. B* **95**, 245408 (2017).
- [77] N. Luo, C. Si, and W. Duan, Structural and electronic phase transitions in ferromagnetic monolayer VS_2 induced by charge doping, *Phys. Rev. B* **95**, 205432 (2017).
- [78] X. Sui, T. Hu, J. Wang, B. Gu, W. Duan, and M. Miao, Voltage-controllable colossal magnetocrystalline anisotropy in single-layer transition metal dichalcogenides, *Phys. Rev. B* **96**, 041410(R) (2017).
- [79] M. A. McGuire, H. Dixit, V. R. Cooper, and B. C. Sales, Coupling of crystal structure and magnetism in the layered, ferromagnetic insulator CrI_3 , *Chem. Mater.* **27**, 612 (2015).
- [80] W. B. Zhang, Q. Qu, P. Zhu, and C. H. Lam, Robust intrinsic ferromagnetism and half semiconductivity in stable two-dimensional single-layer chromium trihalides, *J. Mater. Chem. C* **3**, 12457 (2015).
- [81] H. Wang, F. Fan, S. Zhu, and H. Wu, Doping enhanced ferromagnetism and induced half-metallicity in CrI_3 monolayer, *Euro. Phys. Lett.* **114**, 47001 (2016).
- [82] J. Liu, Q. Sun, Y. Kawazoe, and P. Jena, Exfoliating biocompatible ferromagnetic Cr-trihalide monolayers, *Phys. Chem. Chem. Phys.* **18**, 8777 (2016).
- [83] J. He, S. Ma, P. Lyu, and P. Nachtigall, Unusual Dirac half-metallicity with intrinsic ferromagnetism in vanadium trihalide monolayers, *J. Mater. Chem. C* **4**, 2518 (2016).
- [84] J. L. Lado and J. F. Rossier, On the origin of magnetic anisotropy in two dimensional CrI_3 , *2D Mater* **4**, 035002 (2017).
- [85] M. A. McGuire, Crystal and magnetic structures in layered, transition metal dihalides and trihalides, *Crystals* **7**, 121 (2017).
- [86] Y. Jiao, F. Ma, C. Zhang, J. Bell, S. Sanvito, and A. Du, First-Principles Prediction of Spin-Polarized Multiple Dirac

- Rings in Manganese Fluoride, *Phys. Rev. Lett.* **119**, 016403 (2017).
- [87] J. He, X. Li, P. Lyu, and P. Nachtigall Nanoscale, Near-room-temperature Chern insulator and Dirac spin-gapless semiconductor: Nickel chloridemonolayer, *Nanoscale* **9**, 2246 (2017).
- [88] S. Lin and J. Kuo, Towards the ionic limit of two-dimensional materials: Monolayer alkaline earth and transition metal halides, *Phys. Chem. Chem. Phys.* **16**, 20763 (2014).
- [89] F. Lu, W. Wang, X. Luo, X. Xie, Y. Cheng, H. Dong, H. Liu, and W. Wang, A class of monolayer metal halogenides MX_2 : Electronic structures and band alignments, *Appl. Phys. Lett.* **108**, 132104 (2016).
- [90] V. V. Kulish and W. Huang, Single-layer metal halides MX_2 ($X = \text{Cl, Br, I}$): Stability and tunable magnetism from first principles and Monte Carlo simulations, *J. Mat. Chem. C* **5**, 8734 (2017).
- [91] M. Mushtaq, Y. Zhou, and X. Xiang, NiX_2 ($X = \text{Cl and Br}$) sheets as promising spin materials: A first-principles study, *RSC. Adv.* **7**, 22541 (2017).
- [92] H. Zheng, J. Zheng, C. Wang, H. Han, and Y. Yan, Enhancing the perpendicular magnetic anisotropy of 1T- FeCl_2 monolayer by applying strain: First-principles study, *J. Magn. Magn. Mater.* **444**, 184 (2017).
- [93] P. Giannozzi, S. Baroni, N. Bonini, M. Calandra, R. Car, C. Cavazzoni, D. Ceresoli, G. L. Chiarotti, M. Cococcioni, I. Dabo, A. D. Corso, S. de Gironcoli, S. Fabris, G. Fratesi, R. Gebauer, U. Gerstmann, C. Gougoussis, A. Kokalj, M. Lazzeri, L. Martin-Samos, N. Marzari, F. Mauri, R. Mazzarello, S. Paolini, A. Pasquarello, L. Paulatto, C. Sbraccia, S. Scandolo, G. Sclauzero, A. P. Seitsonen, A. Smogunov, P. Umari, and R. M. Wentzcovitch, QUANTUM ESPRESSO: A modular and open-source software project for quantum simulations of materials, *J. Phys.: Cond. Matter.* **21**, 395502 (2009).
- [94] J. P. Perdew, K. Burke, and M. Ernzerhof, Generalized Gradient Approximation Made Simple, *Phys. Rev. Lett.* **77**, 3865 (1996).
- [95] S. Grimme, Semiempirical GGA-type density functional constructed with a long-range dispersion correction, *J. Comp. Chem.* **27**, 1787 (2006).
- [96] J. P. Perdew and A. Zunger, Self-interaction correction to density-functional approximations for many-electron systems, *Phys. Rev. B* **23**, 5048 (1981).
- [97] N. Marom, J. Bernstein, J. Garel, A. Tkatchenko, E. Joselevich, L. Kronik, and O. Hod, Stacking and Registry Effects in Layered Materials: The Case of Hexagonal Boron Nitride, *Phys. Rev. Lett.* **105**, 046801 (2010).
- [98] B. N. Figgis and M. A. Hitchman, *Ligand Field Theory and its Applications* (Wiley-VCH, New York, 2000).
- [99] See Supplemental Material at <http://link.aps.org/supplemental/10.1103/PhysRevB.101.085415> for the total energy difference, lattice constants, the J coupling parameters along with magnetic moments and transition temperatures using DFT-D2, band structures, the associated density of states and the orbital projected density of states (PDOS) calculated for self-consistently converged magnetic configurations, the carrier density dependent magnetic phase transitions calculated within DFT-D2+ U using an onsite repulsion $U = 4$ eV. We also obtain the heat capacity as a function of temperature through the METROPOLIS Monte Carlo simulation in a 32×64 superlattice.
- [100] J. Chaloupka, G. Jackeli, and G. Khaliullin, Zigzag Magnetic Order in the Iridium Oxide Na_2IrO_3 , *Phys. Rev. Lett.* **110**, 097204 (2013).
- [101] N. Metropolis, A. W. Rosenbluth, M. N. Rosenbluth, and A. H. Teller, Equation of state calculations by fast computing machines, *J. Chem. Phys.* **21**, 1087 (1953).
- [102] M. E. J. Newman and G. T. Barkema, *Monte Carlo Methods in Statistical Physics* (Clarendon Press, Oxford, 1999).
- [103] D. P. Landau and K. Binder, *Monte Carlo Simulations in Statistical Physics* (Cambridge University Press, Cambridge, 2000).
- [104] A. Dal Corso, Pseudopotentials periodic table: From H to Pu, *Comput. Mater. Sci.* **95**, 337 (2014).
- [105] D. Li, A. Smogunov, C. Barreateau, F. Ducastelle, and D. Spanjaard, Magnetocrystalline anisotropy energy of Fe(001) and Fe(110) slabs and nanoclusters: A detailed local analysis within a tight-binding model, *Phys. Rev. B* **88**, 214413 (2013).
- [106] K. Binder and D. P. Landau, Critical properties of the two-dimensional anisotropic Heisenberg model, *Phys. Rev. B* **13**, 1140 (1976).
- [107] F. Matsukura, Y. Tokura, and H. Ohno, Control of magnetism by electric fields, *Nat. Nanotech.* **10**, 209 (2015).
- [108] H. Ohno, D. Chiba, F. Matsukura, T. Omiya, E. Abe, T. Dietl, Y. Ohno, and K. Ohtani, Electric-field control of ferromagnetism, *Nature (London)* **408**, 944 (2000).
- [109] M. Endo, S. Kanai, S. Ikeda, F. Matsukura, and H. Ohno, Electric-field effects on thickness dependent magnetic anisotropy of sputtered $\text{MgO}/\text{Co}_{40}\text{Fe}_{40}\text{B}_{20}/\text{Ta}$ structures, *Appl. Phys. Lett.* **96**, 212503 (2010).
- [110] N. Levy, S. A. Burke, K. L. Meaker, M. Panlasigui, A. Zettl, F. Guinea, A. H. Castro Neto, and M. F. Crommie, Strain-induced pseudo-magnetic fields greater than 300 tesla in graphene nanobubbles, *Science* **329**, 544 (2010).
- [111] B. Hunt, J. D. Sanchez-Yamagishi, A. F. Young, M. Yankowitz, B. J. LeRoy, K. Watanabe, T. Taniguchi, P. Moon, M. Koshino, P. Jarillo-Herrero, and R. C. Ashoori, Massive Dirac fermions and Hofstadter butterfly in a van der Waals heterostructure, *Science* **340**, 1427 (2013).
- [112] C. R. Woods, L. Britnell, A. Eckmann, R. S. Ma, J. C. Lu, H. M. Guo, X. Lin, G. L. Yu, Y. Cao, R. V. Gorbachev, A. V. Kretinin, J. Park, L. A. Ponomarenko, M. I. Katsnelson, Yu. N. Gornostyrev, K. Watanabe, T. Taniguchi, C. Casiraghi, H.-J. Gao, A. K. Geim, and K. S. Novoselov, Commensurate-incommensurate transition in graphene on hexagonal boron nitride, *Nat. Phys.* **10**, 451 (2014).
- [113] J. Jung, A. M. DaSilva, A. H. MacDonald, and S. Adam, Origin of band gaps in graphene on hexagonal boron nitride, *Nat. Commun.* **6**, 6308 (2015).
- [114] M. Yankowitz, J. Jung, E. Laksono, N. Leconte, B. L. Chittari, K. Watanabe, T. Taniguchi, S. Adam, D. Graf, and C. R. Dean, Dynamic band structure tuning of graphene moire superlattices with pressure, *Nature (London)* **557**, 404 (2018).